

A Novel Objective Function DYNO for Automatic Multi-variable Calibration of 3D Lake Models

Wei Xia^{1,2,3}, Taimoor Akhtar⁴, Christine A. Shoemaker^{1,2,3}

¹Department of Civil and Environmental Engineering, National University of Singapore, 117576, Singapore

²Department of Industrial Systems Engineering and Management, National University of Singapore, 117576, Singapore

³Energy and Environmental Sustainability for Megacities (E2S2) Phase II, Campus for Research Excellence and Technological Enterprise (CREATE), 138602, Singapore

⁴RWDI Consulting Engineers and Scientists, N1G 4P6, ON, Canada

Correspondence to: Wei Xia (xiawei@u.nus.edu)

Abstract. This study introduced a novel Dynamically Normalized Objective Function (DYNO) for multi-variable (i.e., temperature and velocity) model calibration problems. DYNO combines the error metrics of multiple variables into a single objective function by dynamically normalizing each variable's error terms using information available during the search. DYNO is proposed to dynamically adjust the weight of the error of each variable hence balancing the calibration to each variable during optimization search. The DYNO is applied to calibrate a tropical hydrodynamic model where temperature and velocity observation data are used for model calibration simultaneously. We also investigated the efficiency of DYNO by comparing the calibration result obtained with DYNO to the result obtained through calibrating to only temperature and to the result obtained through calibrating to only velocity. The result indicates that DYNO can balance the calibration in terms of water temperature and velocity and that calibrating to only one variable (e.g., temperature or velocity) cannot guarantee the goodness-of-fit of another variable (e.g., velocity or temperature) in our case. Our study implies that in practical application, for an accurate spatially distributed hydrodynamic quantification, including direct velocity measurements are likely to be more effective than using only temperature measurements for calibrating a 3D hydrodynamic model. Our example problems were computed with a parallel optimization method PODS but DYNO can also be easily used in serial applications.

1. Introduction

Lake hydrodynamic models simulate the hydrodynamic or thermodynamic processes in lakes and reservoirs that are important for simulating water quality in aquatic eco-systems (Chanudet et al., 2012). These simulation models (e.g., hydrodynamic modelling) play a critical role in managing water bodies, as they are built to support the simulation of the spatial and temporal distributions of specific water quality variables (e.g., nutrients, chlorophyll-a), and to study the response of a water body to different future management scenarios. The parameters of these models usually need to be calibrated to measured data to adequately represent local effects and hydrodynamic processes. Model calibration is a vital step in complex hydrodynamic modelling of lakes and other aquatic systems.

Model calibration of lake hydrodynamic models is mainly done manually (also called trial and error), where experts tune the parameters and simultaneously evaluate the goodness-of-fit between the simulation output and observations. This process is subjective, time-intensive and requires extensive expert knowledge (Afshar et

38 al., 2011; Xia et al., 2021; Solomatine et al., 1999; Fabio et al., 2010; Baracchini et al., 2020). The challenges
39 associated with manual calibration have encouraged the application of auto-calibration to lake hydrodynamic
40 models, where the calibration is set up as an inverse problem to minimize the error between the simulation and
41 observations. Some studies (e.g., Gaudard et al. (2017), Luo et al. (2018), Ayala et al. (2020) and Wilson et al.
42 (2020)) have applied automatic calibration to one-dimensional hydrodynamic lake models where water
43 temperature is the variable that is simulated and calibrated. These one-dimensional models are relatively cheap to
44 run, allowing the use of automatic calibration methods that typically require many simulation evaluations to
45 determine suitable parameter sets (e.g., differential evolution used in Luo et al. (2018) and Monte Carlo sampling
46 used in Ayala et al. (2020)). However, one-dimensional models are unable to simulate the horizontal spatial
47 distribution and cannot capture the 3D processes, and thus may not be suitable for certain studies. Consequently,
48 2-dimensional or 3-dimensional models are preferred for studying the spatial-temporal distribution of water
49 variables and are increasingly used to study lakes around the world (Chanudet et al., 2012; Galelli et al., 2015;
50 Hui et al., 2018; Soullignac et al., 2017; Wahl and Peeters, 2014; Xu et al., 2017; Baracchini et al., 2020) . The
51 calibration of 3-dimensional models, though, is considerably more challenging than calibration of one-
52 dimensional models, since 3-dimensional models are significantly more computationally expensive and also
53 involve more complicated physical processes (such as advection of flows).

54 The computationally expensive character of 3-dimensional lake models makes traditional optimization
55 methods, such as differential evolution and Monte Carlo sampling, unsuitable for automatic calibration because
56 these methods usually require many evaluations to get an acceptable solution. Surrogate-based optimization is
57 highly suitable for such problems (Bartz-Beielstein and Zaefferer, 2017; Lu et al., 2018; Razavi et al., 2012) and
58 recent studies have applied surrogate-based optimization methods to parameter estimation of hydrodynamics
59 models. Surrogate-based optimization methods use a cheap-to-run surrogate approximation model (of the
60 calibration objective) fitted with all known (i.e., already evaluated) values of the original expensive objective
61 function, to guide the optimization search and reduce the number of evaluations required on the expensive
62 simulations. For example, Xia et al. (2021) proposed a new optimization method called PODS (parallel
63 optimization with dynamic coordinate search using surrogates) suitable for computationally expensive problems,
64 and applied it to automatic calibration of a three-dimensional lake hydrodynamic models. More elaborate
65 discussions on surrogate-based optimization algorithms can be found in Xia et al. (2021), Xia and Shoemaker
66 (2021), Razavi et al. (2012), Bartz-Beielstein and Zaefferer (2017) and Haftka et al. (2016).

67 Computational intensity is not the only critical challenge associated with parameter estimation of 3-
68 dimensional lake hydrodynamic models. Parameter estimation of these models is also a multi-site & multi-variable
69 calibration problem, i.e., observation data is usually available at multiple locations and the underlying models
70 simulate multiple variables (e.g., temperature and velocity). Moreover, simultaneous calibration of multiple
71 variables is desired due to complex interactions between the different variables. For instance, temperature and
72 velocity are inter-dependent variables of a lake hydrodynamic model, since water temperature affects the
73 movement of water, and water velocity affects the distribution of water temperature. However, most prior research
74 studies have calibrated hydrodynamic models to only temperature. This might be because temperature
75 measurements are relatively less expensive to get compared with velocity measurements and often temperature
76 measurements are available to help predict water quality phenomena. Wahl and Peeters (2014) use the measured
77 water temperatures to calibrate a 3-dimensional hydrodynamic model of Lake Constance. Kaçikoç and Beyhan

78 (2014) calibrate the temperature of Lake Egirdir hydrodynamic model, the flow simulation of which is used for
79 the lake water quality modeling. Marti et al. (2011) and Xue et al. (2015) also only used temperature data for lake
80 hydrodynamic model calibration. Moreover, these studies use manual calibration for parameter estimation. Xia et
81 al. (2021) use automatic calibration for parameter estimation, but only use water temperature observations in the
82 calibration process. Reproducing water level is also a parameter estimation approach that pseudo-considers flow
83 dynamics in calibration; however, a calibrated model that correctly simulates observed water level does not
84 necessarily reproduce the observed 3D flow field accurately (Wagner and Mueller, 2002; Parsapour-Moghaddam
85 and Rennie, 2018). Amadori et al. (2021) investigated the use of different sources of temperature data (from in-
86 suite observations, multi-site high-resolution profiles and remote sensing data) to compensate for the scarcity of
87 velocity measurements. This is a practicable approach when there is no velocity data available and there are such
88 different sources of temperature data available. However, when there is no high-quality remote sensing data (for
89 example, because of cloud) or a large amount of high-resolution profiles of temperature measurement it is still
90 challenging to verify the spatial simulation of hydrodynamic quantities.

91 Lake hydrodynamic models predict the velocities throughout a water body. Accurate velocity simulations
92 are thus important to understand the spatial distribution of water quality problems (e.g., algal blooms) in sizeable
93 lakes. Hence, during the calibration of these models, it is useful to know whether efforts to measure velocity
94 directly are justifiable even if temperature data is already available. We will examine the extent to which direct
95 measurement of velocities justifies the extra effort by giving more accurate results for hydrodynamics models.
96 We will also look at the error of the spatial distribution of hydrodynamics associated with calibrating to
97 temperature only, which is rarely studied in the literature.

98 There are a few studies that attempt to calibrate lake hydrodynamic models to both temperature and
99 velocity. Chanudet et al. (2012) attempt to calibrate both temperature and velocity sequentially (using manual
100 calibration), i.e., they calibrate water temperature first and then the current velocities. Baracchini et al. (2020)
101 performed two sequential steps in the automatic calibration of temperature and velocity, and the velocity
102 calibration is based on the results obtained from temperature calibration. However, one problem with such two-
103 step sequential approaches, either by manual or auto-calibration, is that the calibration of the second variable
104 might significantly alter the calibration quality of the first variable. This is especially true for multi-variable
105 calibration problems, where the multiple variables being calibrated are sensitive to the parameters being
106 calibrated. Other examples of such multi-variable calibration problems include watershed model calibration
107 (Franco et al., 2020) and seawater intrusion model calibration (Coulon et al., 2021), among others. These multi-
108 variable problems require calibration frameworks that allow simultaneous calibration of all variables rather than
109 calibrating one and then the second.

110 There are prior studies that simultaneously calibrate both temperature and velocity variables of
111 hydrodynamic models. However, these use a trial and error (manual) mechanism for calibration (Råman Vinnå et
112 al., 2017; Soullignac et al., 2017; Jin et al., 2000; Paturi et al., 2014). Manual calibration of multiple hydrodynamic
113 variables simultaneously, is even harder than calibration of a single variable. A key challenge for automatic
114 calibration of multi-variable calibration problems is in defining a suitable objective function. Traditional
115 approaches typically formulate the goodness-of-fit of multiple variables into a single objective function by adding
116 weights between the goodness-of-fit of multiple variables and solve the problem with single objective
117 optimization (SOO) techniques (Afshar et al., 2011; Pelletier et al., 2006). However, a drawback of this approach

118 is that the relative error magnitude of each variable of the new solutions found will probably vary during the
 119 search making it difficult to determine appropriate weights since they need to be determined / defined *a priori*, i.e.,
 120 before optimization.

121 Another approach for calibration of multi-variables is using multi-objective optimization (MOO)
 122 techniques (Afshar et al., 2013). However, multi-objective techniques are commonly used to optimize multiple
 123 sub-objectives that have a trade-off between each sub-objective (Akhtar and Shoemaker, 2016; Reed et al., 2013;
 124 Alfonso et al., 2010; Giuliani et al., 2016; Herman et al., 2014). While for the multi-variable hydrodynamic
 125 calibration problems, it is not apparent that there is usually a trade-off between the fit of multiple variables.
 126 Moreover, MOO is considerably more computationally difficult than SOO and typically requires many more
 127 objective function evaluations. Thus, MOO may not be desired for computationally expensive calibration
 128 problems, especially when a significant trade-off between the objectives may not be present. Consequently, multi-
 129 variable calibration utilizing efficient SOO algorithms, while balancing the calibration to each variable equally
 130 during calibration, is a research area of significant value.

131 We introduce a new Dynamically Normalized Objective Function (DYNO) for automatic multi-variable
 132 calibration. The error of each variable (e.g., temperature and velocity of hydrodynamic models) is dynamically
 133 normalized by using the information about variable error of the evaluations found during the optimization search
 134 process. In this way, the balance between the calibration of each variable is dynamically adjusted. We tested the
 135 efficiency of DYNO on a computationally expensive hydrodynamic lake model of a tropical reservoir, which
 136 takes 5 hours to run per simulation. DYNO is coupled into a recent parallel surrogate optimization algorithm,
 137 PODS (Xia et al., 2021), and successfully applied for the calibration of multiple variables of the hydrodynamic
 138 model. Using DYNO, we investigate the impact of using temperature and/or velocity observations on model
 139 accuracy. Since velocity measurements are usually not included in standard lake monitoring systems (whereas
 140 temperature measurements are included), real velocity observations are seldom available (Amadori, et al, 2021).
 141 Real observations for velocity are not available in our case as well. Hence, we conducted our investigation based
 142 on synthetic observations generated from a calibrated model. It is worthwhile to revisit and validate this analysis
 143 with real velocity measurements if they are available in the future.

144 2. Methodology

145 2.1 Multi-variable Calibration Problems Description

146 The calibration problems investigated in this study are multi-site (i.e., observations are available from multiple
 147 locations), multi-variable (e.g., temperature and velocity for hydrodynamics) problems, and are defined
 148 mathematically as follows (the variable and function definition are given in Table 1):

$$149 \min_{\mathbf{X} \in \Theta} F(\mathbf{X}|\mathbf{K}) = F(\{f_k(\mathbf{X})|k \in \mathbf{K}\}) \quad (1)$$

$$150 f_k(\mathbf{X}) = f_k(\{g_j(\mathbf{Sim}_j^k(\mathbf{X}), \mathbf{Obs}_j^k)|j = 1, \dots, M\}) \quad (2)$$

151 Note that the notation $\{z_i\}$ in Eq. (2) is simply meant to imply the function on the left depends on the finite series
 152 of quantities inside the braces $\{\bullet\}$.

153 **Table 1.** Notation and definitions of variables and functions in Eq. (1) and (2).

Variable	Description
----------	-------------

\mathbf{K}	The set of variables whose observation data is used in calibration. For example, $\mathbf{K} = [Tem]$ means that water temperature observation is used for calibration, i.e., water temperature is the variable that is being calibrated; $\mathbf{K} = [\overline{Vel}]$ means velocity observation is used for calibration; $\mathbf{K} = [Tem, \overline{Vel}]$ means that both temperature and velocity observations are used for model calibration
k	The symbol for elements in \mathbf{K} variable (e.g., water temperature or velocity, $k = Tem$ or $k = \overline{Vel}$). $k \in \mathbf{K}$
\mathbf{X}	A d dimensional parameter vector restricted to parameter space Θ , where d is the number of parameters to be optimized. $\mathbf{X} = (x_1, x_2, \dots, x_d)$.
Θ	The parameter space is defined by the upper and lower limits on each parameter (\mathbf{X}^{max} and \mathbf{X}^{min} , respectively)
M	The total number of observation locations (or sites).
j	The index for observation location. $j = 1, \dots, M$
$Sim_{t,j}^k(\mathbf{X})$	The simulation output of variable k at location j at time step t given the parameter vector \mathbf{X}
$Obs_{t,j}^k$	The observation (data) of variable k at location j at time step t .
$Sim_j^k(\mathbf{X})$	The simulation time series output of variable k at location j at times $t = 1, \dots, N$ given the parameter vector \mathbf{X} . $Sim_j^k(\mathbf{X}) = (Sim_{1,j}^k(\mathbf{X}), \dots, Sim_{N,j}^k(\mathbf{X}))$.
Obs_j^k	The observation (data) time series of variable k at location j at times $t = 1, \dots, N$. $Obs_j^k = (Obs_{1,j}^k, \dots, Obs_{N,j}^k)$.
N	The total time steps of the observation data
t	The index for time steps. $t = 1, \dots, N$
Function	Description
$F(\mathbf{X} \mathbf{K})$	The calibration objective function given the observation data of variables in \mathbf{K} for calibration. $F(\mathbf{X} \mathbf{K})$ is a composite function of $f_k(\mathbf{X})$
$f_k(\mathbf{X})$	The error function of variable k over multiple site. $f_k(\mathbf{X})$ is a composite function of $g_j(Sim_j^k(\mathbf{X}), Obs_j^k)$ for sites $j = 1, \dots, M$
$g_j(Sim_j^k(\mathbf{X}), Obs_j^k)$	Goodness of fit between time series simulation output $Sim_j^k(\mathbf{X})$ and observation Obs_j^k of variable k at location j . When $k = Tem$, Normalized Root Mean Square Error (NRMSE) is utilized for $g_j(\bullet)$. When $k = \overline{Vel}$, normalized Fourier Norms of Root Mean Square Error (FNs) is used for $g_j(\bullet)$.

154

155 The set of parameters \mathbf{X} being calibrated in this study includes nine parameters ($d = 9$). Details of these
156 parameters are provided in Table 2 in section 2.4. The two variables calibrated in this study are velocity and
157 temperature, for which data exists for different spatial locations and time points.

158 We investigate different calibration formulations, where either one or both of these variables are
159 calibrated. Consequently, $\mathbf{K} = [Tem]$ means that water temperature observation is used for calibration, i.e., water
160 temperature is the variable that is being calibrated; $\mathbf{K} = [\overline{Vel}]$ means velocity observation is used for calibration;
161 $\mathbf{K} = [Tem, \overline{Vel}]$ means that both temperature and velocity observations are used for model calibration, i.e., both
162 variables are being calibrated simultaneously. The objective function in each scenario is discussed in section 2.5.

163 2.2 DYNO for Model Calibration with Multiple Variables

164 One major issue for model calibration with multiple variables is how to formulate the error of multiple variables
165 with a single objective function. In practice, different variables (e.g., temperature and velocity) usually have
166 different physical units and magnitudes of error. Their error functions cannot be summed up directly into a single
167 objective function if we wish to give the error of each variable an equal weight in the overall objective function.

168 The respective error functions have to be normalized. There are goodness-of-fit metrics that can normalize the
 169 error of different variables (for example, Normalized Root Mean Square Error (NRMSE) and Kling-Gupta
 170 Efficiency (KGE, (Gupta et al., 2009))). However, it is still possible that the highest attainable value (or
 171 distribution) of NRMSE (or KGE) across the parameter space for one variable maybe be much higher than the
 172 highest attainable value (or distribution) of NRMSE (or KGE) of another variable. Hence, how to balance such
 173 differences among multiple variables is still important even when the normalized goodness-of-fit metrics are used.

174 We propose a new general objective function, DYNO, for the multi-variable calibration problem. Let $\boldsymbol{\psi}$
 175 be the set of evaluations found so far by the optimization, DYNO (as shown in Eq. (3)) normalizes the error of
 176 each variable $f_k(\mathbf{X})$ with its upper and lower bound, f_k^{max} and f_k^{min} of all evaluations in $\boldsymbol{\psi}$. Since true values of
 177 bounds are not known, f_k^{max} and f_k^{min} are dynamically updated during the optimization search after each iteration.
 178 The Mathematical formulation of the multi-variable calibration problem, with DYNO, is as follows:

$$179 \min F(\mathbf{X}|\mathbf{K}) = \sum_{k \in K} \frac{f_k(\mathbf{X}) - f_k^{min}(\mathbf{X})}{f_k^{max}(\mathbf{X}) - f_k^{min}(\mathbf{X})} \quad (3)$$

$$180 f_k^{max}(\mathbf{X}) = \max\{f_k(\mathbf{X}) \text{ for all } \mathbf{X} \in \boldsymbol{\psi}\} \quad (4)$$

$$181 f_k^{min}(\mathbf{X}) = \min\{f_k(\mathbf{X}) \text{ for all } \mathbf{X} \in \boldsymbol{\psi}\} \quad (5)$$

182 where $f_k^{max}(\mathbf{X})$ and $f_k^{min}(\mathbf{X})$ are the maximum and minimum values of $f_k(\mathbf{X})$ for all evaluations in $\boldsymbol{\psi}$. $f_k^{max}(\mathbf{X})$
 183 and $f_k^{min}(\mathbf{X})$ have to be updated dynamically in each iteration during optimization. The detailed description of
 184 the implementation of Eq. (3) in the algorithm (i.e., PODS) tested in this study is given in Section 2.6 (the
 185 Algorithm Description section).

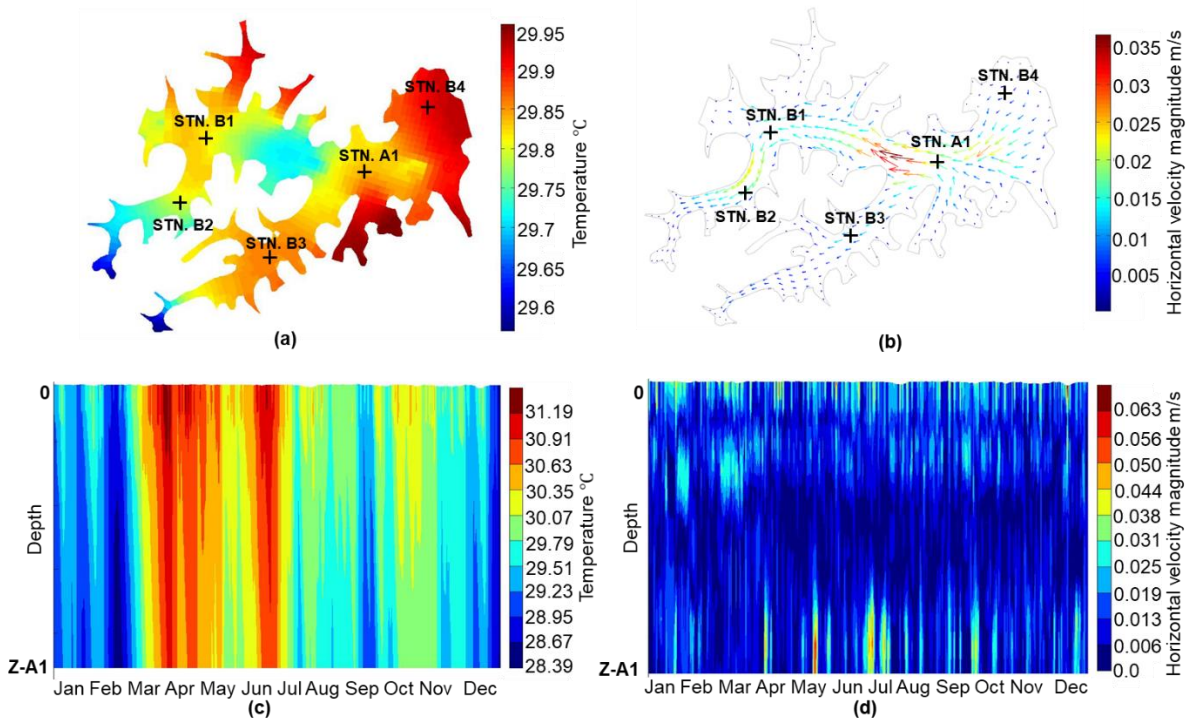
186 2.3 Study Site and Data

187 We use a 3-dimensional model of a tropical reservoir as an example to test the efficiency of DYNO for multi-
 188 variable calibration problems and to study the impact of using temperature and/or velocity data for model
 189 calibration. The horizontal boundary of the studied reservoir is given in Fig. 1 (a) and (b). The reservoir has over
 190 250 ha of water surface with a maximum depth of about 22 meters. One online water quality profiler station (STN.
 191 A1) was installed in the middle of the reservoir. The water temperature data at the station are available at various
 192 depths. The model is built for the simulation of the year 2013. One-year measured temperature data was used for
 193 model calibration in a previous study (Xia et al., 2021). We use this calibrated model to create synthetic
 194 observation data since the real velocity measurements are not available. We first assume a set of “true” model
 195 parameters \mathbf{X}^R . The value of \mathbf{X}^R is based on manual calibration by experts and is listed in Table 2. The spatial
 196 and temporal observation data for the hypothetical lake is synthetically generated based on the “true” model
 197 parameters \mathbf{X}^R . The synthetic observation data for the hypothetical temperate lake is generated by running the
 198 simulation model for one year with the vector of model parameters \mathbf{X}^R . The simulation output is then saved hourly
 199 in N time steps for multiple variables, i.e., temperature and velocity ($\mathbf{K} = [Tem, \overline{Vel}]$) at M locations (specified
 200 in Fig. 1). In our study case, $N = 8761$ and $M = 12$ with different depths of five hypothetical sensor stations
 201 (STN. A1 and STN. B1-4 as shown in Fig. 1 (a) and (b)).

202 The saved hourly simulated output time series is denoted as $\Gamma = \{\mathbf{Sim}_j^k(\mathbf{X}^R), k \in \mathbf{K} = [Tem, \overline{Vel}], j =$
 203 $1, \dots, M\}$, which as defined (in Table 1) contains information for each time step, $t = 1, \dots, N$. So Γ is used as

204 observation data for model calibration, i.e., $Obs^k, k \in K = [Tem, \overline{Vel}]$ in Eq. (1). In the test of optimization for
 205 calibration, the true values of the parameter vector X^R are not provided to the optimization. The optimization will,
 206 instead, search for the best set of X that will minimize the objective function $F(X|K)$, where $K =$
 207 $[Tem], [\overline{Vel}], or [Tem, \overline{Vel}]$. So the goal of automatic calibration via optimization is to obtain an optimum
 208 calibration X^* that results in simulation model output, $Sim_j^k(X), k \in K, j = 1, \dots, M$, (see Eq. (1) and Eq. (2)) that
 209 is close to the synthetic observation time series data in Γ .

210 The temperature and velocity simulation results at the year 2013 based on the “true” model parameters
 211 (shown in Table 2) show temporal and spatial variation, as shown in Fig. 1 (a)-(d). Figure 1 (a) and (b) show the
 212 temperature and horizontal velocity distribution at the surface layer. Figure 1 (c) and (d) show the distribution of
 213 temperature and velocity magnitude at STN. A1. There is obvious temperature stratification in the vertical
 214 direction (as shown in Fig. 1(c)). We have five sampling locations across the reservoir. The observation data at
 215 these five locations are used to calibrate the model parameters.



216
 217 **Figure 1.** Hydrodynamic model simulation result (with “true” model parameters) at the year 2013. (a) Simulated
 218 temperature spatial distribution with sampling locations. (b) Simulated velocity spatial distribution with sampling
 219 locations. (c) Time-depth plot of simulated temperature at STN. A1. (d) Time-depth plot of velocity magnitude at
 220 STN. A1. Z-A1 is the maximum water depth at station A1.

221 2.4 Hydrodynamic Model and Calibration Parameters

222 The description of the hydrodynamic model is given in (Xia et al., 2021). The hydrodynamic model is built with
 223 Delft3D-FLOW (Hydraulics, 2006). The Delft3D-Flow hydrodynamic model used was set up by the water
 224 utilities’ employees and consultants, including the domain construction, input data preparation, and model
 225 configuration. The grid coordinate system is based on Cartesian coordinates (Z-grid), which has horizontal
 226 coordinate lines that are almost parallel with density interfaces to reduce the artificial mixing of scalar properties
 227 such as temperature. The number of grid points in the x-direction is 65, the number of grid points in the y-direction

228 is 67, and the number of layers in vertical is 19. A single 1-year simulation takes about 5 hours to run in serial on
 229 a windows desktop with CPU Intel Core i7-4790.

230 There are nine tunable model parameters (listed in Table 2) in the model. The first five parameters in
 231 Table 2 are related to the turbulence calculation. The k- ϵ closure model (Uittenbogaard et al., 1992) was chosen
 232 as the turbulence closure model to calculate the viscosity and diffusivity of the water. The calculation of the
 233 viscosity and diffusivity involves five parameters: 1) background viscosity in horizontal ν_H^{back} , 2) vertical ν_V^{back} ,
 234 3) the background eddy diffusivity in horizontal D_H^{back} , 4) vertical D_V^{back} and 5) the Ozmidov length L_{oz} . These
 235 parameters affect both the velocity and the temperature. The vertical exchange of horizontal momentum and mass
 236 is affected by vertical eddy viscosity and eddy diffusivity coefficients (Elhakeem et al., 2015). The horizontal
 237 velocities are affected by the horizontal eddy viscosity and diffusivity coefficients (Chanudet et al., 2012).
 238 Chanudet et al. (2012) highlighted that the most impactful parameter for temperature is the background vertical
 239 eddy viscosity and the Ozmidov length L_{oz} also has a significant effect on the thermal stratification by affecting
 240 the vertical temperature mixing.

241 The next three parameters in Table 2 are related to the simulation of surface heat flux. In the heat flux
 242 model, the evaporative heat flux and heat convection by forced convection are parameterized by the Dalton
 243 number c_e and Stanton number c_H , respectively, which are also in the list of calibration parameters. The Secchi
 244 depth H_{Secchi} (also included in Table 2) is another parameter required by the Ocean heat flux model. Secchi depth
 245 is related to the transmission of radiation in deeper water and thus affects the vertical distribution of heat in the
 246 water column (Chanudet et al., 2012). Heat fluxes through the reservoir bottom were not simulated in the current
 247 model. The last parameter is the Manning coefficient, which affects the roughness of the bottom of the lake and
 248 has a direct impact on velocity.

249 All these nine parameters affect (either directly or indirectly) the thermal and current activity in the water
 250 body. These are also the parameters included in the routine model calibration by local experts and thus, are
 251 included in the calibration process in our study. The calibration range for these parameters (given in Table 2) is
 252 suggested by Singapore water utilities employees and consultants. Some of these parameters might be
 253 spatiotemporally variant (such as Secchi depth, Ozmidov length scale, Dalton number, and Stanton number).
 254 Considering these parameters as time or space-varying parameters will substantially increase the number of
 255 decision variables in optimization. Considering that the reservoir in our study is relatively small and is located in
 256 a tropical region where there is no significant seasonal variation, we **consider these** parameters to be constant
 257 across space and time.

258 **Table 2.** Model parameters used in calibration. X^R denotes the true solution used to generate synthetical
 259 temperature and velocity observations at multi-sites.

Parameter vector X	Parameter	Description (unit)	Physical process	Range	X^R
x_1	ν_H^{back}	Background viscosity in horizontal (m^2/s)	3D turbulence	0.1-1.0 ^{a,b,d,e}	0.5
x_2	D_H^{back}	Background eddy diffusivity in horizontal (m^2/s)		0.1-1.0 ^{a,b,d,e}	0.5
x_3	ν_V^{back}	Background viscosity in vertical (m^2/s)		0-0.005 ^{a,b,c,e}	5.00E-05

x_4	D_V^{back}	Background eddy diffusivity in vertical (m ² /s)		0-0.005 ^{a,b,c,e}	5.00E-05
x_5	L_{oz}	Ozmidov length scale (m)		0-0.05 ^{a,b,e}	0.015
x_6	H_{Secchi}	Secchi depth (m)	Heat flux	0.1-2.0 ^{a,e,f}	1
x_7	c_e	Dalton number (-)		0.001-0.002 ^{a,b,c,e}	0.0013
x_8	c_H	Stanton number (-)		0.001-0.002 ^{a,b,c,e}	0.0013
x_9	n	Manning coefficient (m ^{-1/3} s)	Roughness	0.02-0.03 ^{a,b,e}	0.022

260 ^aDeltares (2014); ^bChanudet et al. (2012); ^cWahl and Peeters (2014); ^dRåman Vinnå et al. (2017); ^eSoullignac et
261 al. (2017); ^fPijcke (2014)
262

263 2.5 Calibration Problem Formulation

264 Three scenarios are considered to investigate the impact of model calibration against temperature and/or velocity
265 observations (as discussed in section 2.1). The first two scenarios calibrate to only one variable, and the last
266 scenario calibrates both variables simultaneously. This section gives the detailed calibration formulations of these
267 three scenarios.

268 2.5.1 Model Calibration with One Variable

269 The objective functions for Cali-Tem and Cali-Vel scenarios are summarized in Eq. (6)-(8) and Eq. (9)-(11),
270 respectively, where only observations of one variable are included in the calibration.

$$271 F(\mathbf{X}|\mathbf{K} = [Tem]) = f_{Tem}(\mathbf{X}) \quad (6)$$

$$272 f_{Tem}(\mathbf{X}) = \sum_{j=1}^M NRMSE_j^{Tem}(\mathbf{X}) \quad (7)$$

$$273 NRMSE_j^{Tem}(\mathbf{X}) = \frac{\sqrt{\frac{1}{N} \sum_{t=1}^N [Sim_{t,j}^{Tem}(\mathbf{X}) - Obs_{t,j}^{Tem}]^2}}{\frac{1}{N} \sum_{t=1}^N Obs_{t,j}^{Tem}} \quad (8)$$

$$274 F(\mathbf{X}|\mathbf{K} = [Vel]) = f_{Vel}(\mathbf{X}) \quad (9)$$

$$275 f_{Vel}(\mathbf{X}) = \sum_{j=1}^M FNS_j^{Vel}(\mathbf{X}) \quad (10)$$

$$276 FNS_j^{Vel}(\mathbf{X}) = \frac{\sqrt{\frac{1}{N} \sum_{t=1}^N \|Sim_{t,j}^{Vel}(\mathbf{X}) - Obs_{t,j}^{Vel}\|_2^2}}{\sqrt{\frac{1}{N} \sum_{t=1}^N \|Obs_{t,j}^{Vel}\|_2^2}} \quad (11)$$

277 where, $NRMSE_j^{Tem}(\mathbf{X})$ and $FNS_j^{Vel}(\mathbf{X})$ denote the Normalized Root Mean Square Error (NRMSE) of
278 temperature (described in Eq. (8)), and normalized Fourier Norms (FNs) of velocity vectors (described in Eq.
279 (11)) at locations j . $Sim_{t,j}^{Vel}(\mathbf{X})$ and $Obs_{t,j}^{Vel}$ denote the simulated velocity given a parameter vector \mathbf{X} and observed
280 velocity, respectively, at time step t and location j . $Sim_{t,j}^{Vel}(\mathbf{X})$ and $Obs_{t,j}^{Vel}$ are 3-dimensional vector. $\|-\|_2$ in Eq.
281 (11) is the Euclidean norm used to quantify the size of a vector.

282 The temperature and velocity data are taken at different depths of multiple stations, and their magnitude
283 at different locations might be different due to spatial variation. Hence, the fitness at each location should be
284 normalized before being summed into the objective function. For water temperature, Normalized Root Mean
285 Square Error (NRMSE, as described in Eq. (8)) is used to quantify and normalize the error between the simulated
286 and observed data. For velocity, normalized Fourier Norms of RMSE (FNs, as described in Eq. (11)) are used to

287 measure the error between the model-simulated and observed data (corresponding simulated and observed
 288 velocity data points are three-dimensional vectors). The calculation of the Fourier Norm follows the description
 289 in Beletsky et al. (2006), Huang et al. (2010), Paturi et al. (2014), and Răman Vinnă et al. (2017).

290 2.5.2 DYNO for Model Calibration with Multiple Variables

291 In the Cali-Both scenario, both temperature and velocity are calibrated simultaneously, which can be treated as a
 292 bi-objective function problem. The objective function in the Cali-Both scenario (as shown in Eq. (12)) applies the
 293 DYNO proposed in Eq. (3). The error functions for water temperature, i.e., $f_{Tem}(\mathbf{X})$, and velocity, i.e., $f_{\vec{Vel}}(\mathbf{X})$,
 294 are the objective functions of the Cali-Tem scenario (Eq. (7) and the Cali-Vel scenario (Eq. (10), respectively.
 295 The temperature and velocity errors are dynamically normalized with their upper and lower bounds during the
 296 search of the optimization algorithm before being summed into a single objective function. The mathematical
 297 formulation of the objective function in the Cali-Both Scenario (based on Eq. (3)) is as follows:

$$298 F(\mathbf{X}|\mathbf{K} = [Tem, \vec{Vel}]) = \frac{f_{Tem}(\mathbf{X}) - f_{Tem}^{min}(\mathbf{X})}{f_{Tem}^{max}(\mathbf{X}) - f_{Tem}^{min}(\mathbf{X})} + \frac{f_{\vec{Vel}}(\mathbf{X}) - f_{\vec{Vel}}^{min}(\mathbf{X})}{f_{\vec{Vel}}^{max}(\mathbf{X}) - f_{\vec{Vel}}^{min}(\mathbf{X})} \quad (12)$$

299 where the maximum and minimum of $f_{Tem}(\mathbf{X})$ and $f_{\vec{Vel}}(\mathbf{X})$ are updated after each optimization iteration (since
 300 new parameter sets are sampled in each optimization iteration). As the number of iterations increases, the
 301 denominators in Eq. (12) also increase since the optimization method finds better minimum objective function
 302 values. Hence the individual objective function components (for each variable) scale dynamically to maintain an
 303 approximately equal weight of the terms related to temperature and velocity.

304 As defined in Eq. (6) to Eq. (12), three calibration formulations are investigated in this study. Table 3
 305 gives a summary of these calibration formulations.

306 **Table 3.** Summary of Objective function formulations for different calibration scenarios.

Scenario Name	Variables used for calibration	Objective Function	Objective Function Formula
Cali-Tem	Temperature	$F(\mathbf{X} \mathbf{K} = [Tem])$	Eq. (6)~(8)
Cali-Vel	Velocity	$F(\mathbf{X} \mathbf{K} = [\vec{Vel}])$	Eq. (9)~(11)
Cali-Both	Temperature and Velocity	$F(\mathbf{X} \mathbf{K} = [Tem, \vec{Vel}])$	Eq. (12)

307 2.6 Implementation of DYNO with PODS

308 In this section, we describe the implementation details for incorporating DYNO into a new efficient parallel
 309 surrogate optimization algorithm, PODS (described in Fig. 2). PODS (Xia et al., 2021) is a parallel version of the
 310 serial DYCORS (DYnamic COordinate search using Response Surface models) algorithm introduced by (Regis
 311 and Shoemaker, 2013). DYCORS is an iterative surrogate method (such methods are sometimes also called
 312 Response Surface Optimization methods, where cheap surrogates of the expensive objective are built to improve
 313 optimization efficiency), designed for optimization of computationally expensive black-box functions within a
 314 limited number of evaluations. DYCORS uses RBF (Radial Basis Function) as surrogates to efficiently explore
 315 the parameter space and propose promising new solutions for expensive evaluation in each algorithm iteration.
 316 The RBF-guided search methodology of DYCORS is designed for high-dimensional black-box optimization

317 within a limited number of evaluations of computationally expensive real objective functions. PODS, like
 318 DYCORS, is designed for black-box optimization problems that are high-dimensional and computationally
 319 expensive and have multiple local minima. Xia et al. (2021) show that PODS is considerably more efficient than
 320 other parallel global optimization methods in obtaining good solutions with fewer objective function evaluations,
 321 which is very important for expensive objective functions like hydrodynamics models. PODS parallelized the
 322 serial DYCORS algorithm by following the Master-worker framework (as shown in Fig. 2). This parallelization
 323 strategy of the algorithm allows simultaneous function evaluations on multiple processors (cores) in batch mode,
 324 which **reduces** the wall-clock time of the optimization process. This can greatly speedup the calibration of
 325 computationally expensive models and make the calibration of some extremely expensive models computationally
 326 tractable.

327 The PODS algorithm begins the optimization from an initial experiment design where a random initial
 328 set of evaluation points are generated with the Latin Hypercube Design (LHD). These evaluation points are
 329 distributed randomly to P workers for simulation evaluations. Each worker will calculate the error/ objective
 330 function of each variable $\{f_k(\mathbf{X}_i) | k \in \mathbf{K}\}$ based on Eq. (2) and return them back to the master. This step (W3 in
 331 Fig. 2) for DYNO-based PODS is different from the original PODS. In the original PODS, only the final objective
 332 function value (instead of **the** error of each variable) is returned to the master.

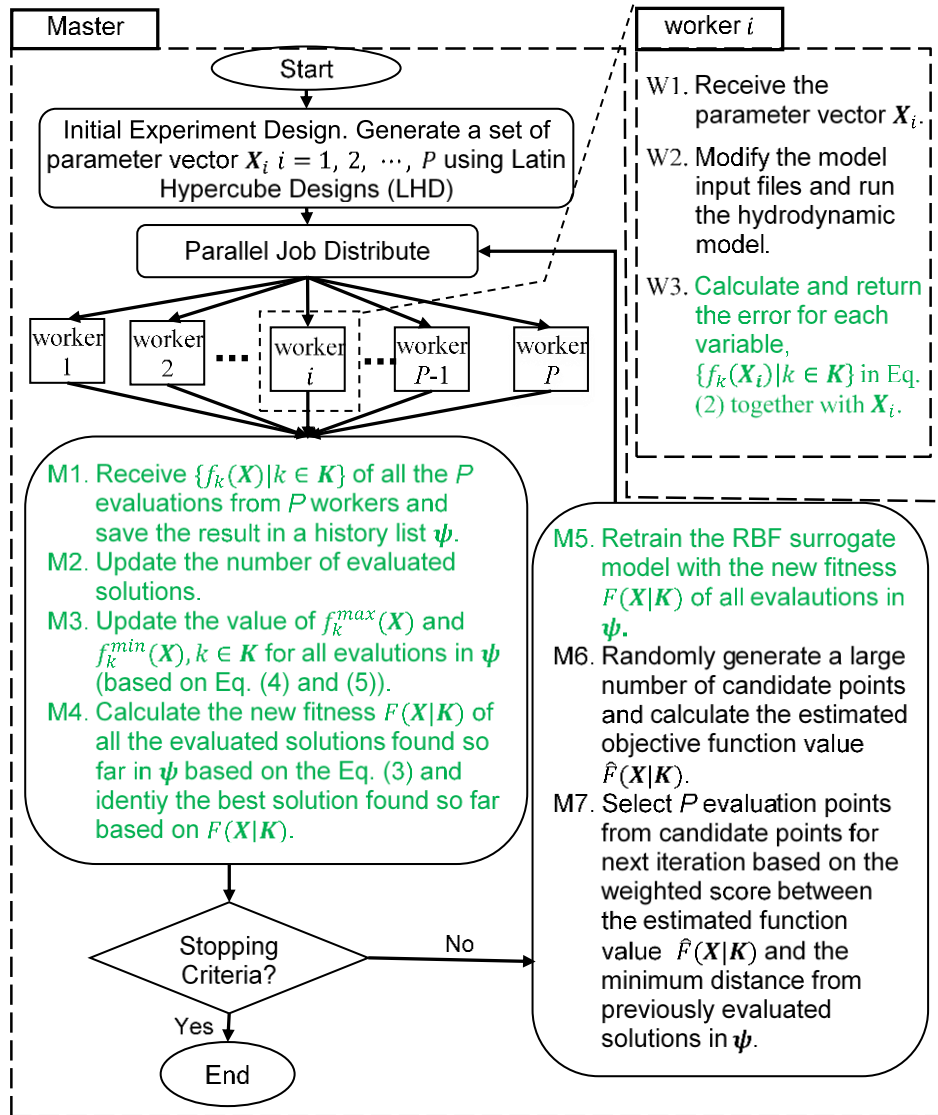
333 After the master collects the result of all the P evaluations, it will add these new results into the history
 334 list $\boldsymbol{\psi}$ that saves all evaluation results found in previous iterations. The history list of $\boldsymbol{\psi}$ is not in the original
 335 PODS and it is necessary for the calculation of the DYNO objective function ($F(\mathbf{X}|\mathbf{K}), \mathbf{X}$) (as shown in Eq. (3)).
 336 For instance, the maximum and minimum value of the error of each variable $f_k^{max}(\mathbf{X})$ and $f_k^{min}(\mathbf{X})$ are
 337 dynamically changing with the increase of the history list $\boldsymbol{\psi}$. The objective function value $F(\mathbf{X}|\mathbf{K})$ for all
 338 evaluations found in current and previous iterations need to be recalculated because of the update of $f_k^{max}(\mathbf{X})$ and
 339 $f_k^{min}(\mathbf{X})$. And the best solution found so far is identified based on the newly calculated $F(\mathbf{X}|\mathbf{K})$. When only one
 340 variable (e.g., temperature or velocity) is considered in the objective function, the best solution is the evaluation
 341 with the lowest error between the simulation output and observations of the variable considered. In cases where
 342 multiple variables are considered in calibration, the best solution should be the evaluation with the smallest value
 343 of $F(\mathbf{X}|\mathbf{K})$ after considering the error of multiple variables (as shown in Eq. (3)). Because the objective function
 344 value for all evaluations in $\boldsymbol{\psi}$ **changed after each iteration**, the RBF is also rebuilt with these new objective
 345 function values of all evaluated solutions ($F(\mathbf{X}|\mathbf{K}), \mathbf{X}$). The rebuilt RBF surrogate is used for the generation of the
 346 evaluation points for the next iteration.

347 PODS with DYNO implementation uses the RBF surrogate in the same way as the original PODS does.
 348 PODS first generates a large number of candidate points around the best solution found so far (refer to Section
 349 2.2 in Xia et al (2021)). The algorithm then selects P evaluation points from these candidate points based on their
 350 estimated objective function $\hat{F}(\mathbf{X}|\mathbf{K})$ based on the RBF surrogate and the minimum distance from all previous
 351 evaluation solutions in $\boldsymbol{\psi}$. A lower estimated objective function $\hat{F}(\mathbf{X}|\mathbf{K})$ is better since it **is** more likely to lead to
 352 solutions with lower objective function value. Meanwhile, candidate points that are far from previous solutions
 353 are also preferred since they help the algorithm to explore regions of the solution domain that **were not** explored
 354 in previous iterations. These unexplored regions could possibly be regions where better solutions are located. The
 355 consideration of estimated objective function $\hat{F}(\mathbf{X}|\mathbf{K})$ and distance information are both considered when

356 selecting the candidate points through a weighted score based on these two aspects. For detailed information on
 357 the implementation of evaluation point selection criteria, one can refer to Section 2.3 in Xia et al (2021). The
 358 selected P evaluation points are then distributed to P workers for evaluations, and the iteration loop continues
 359 until the stopping criteria are met (e.g., the computing budget is finished.)

360 In summary, the implementation of DYNO affects the selection of the best solution found so far and also
 361 the surrogate model (These steps are W3 and M1-5, as highlighted in green color in Fig. 2). We should highlight
 362 that the fitting of the surrogate model is computationally inexpensive compared with the runtime of the expensive
 363 objective function. Hence it does not affect the overall algorithm runtime.

364



365 **Figure 2.** Diagram of the implementation of DYNO with the parallel algorithm PODS. P is the number of
 366 processors available. The green texts (i.e., steps W3, M1-5) are changes made on PODS to incorporate DYNO.
 367 The rest part follows the original PODS method.
 368

369 2.7 Experiments Setup

370 All computational experiments in this study are implemented on a single node on the National Supercomputer
 371 Center (NSCC) of Singapore, which is a Linux-based platform with dual Intel Xeon E5-2690 v3 Processors, with
 372 each node having 24 cores. Hence, we set the number of processors P to be 24. Due to the stochastic nature of the

373 optimization algorithm (i.e., PODS) used in this study, multiple optimization runs are executed for each calibration
374 experiment in Table 3. Considering that the calibrated hydrodynamic model in this study is extremely expensive,
375 we perform three optimization trials for each calibration experiment (see Table 3 for a list of experiments).
376 Furthermore, to remove any initial sampling bias, each concurrent optimization trial for the three calibration
377 experiments is initialized with the same Latin Hypercube experimental design (so the calibration in each scenario
378 **starts** from the same initial solutions). We also investigated the performance of different forms of DYNO on the
379 Cali-Both scenario.

380 We set the same evaluation budget (i.e., the maximum number of hydrodynamic model runs) for each
381 trial and calibration scenario (i.e., Cali-Tem, Cali-Vel, and Cali-Both). The maximum number of hydrodynamic
382 model runs in each trial is 192, **which is 8 iterations** with 24 evaluations in each iteration. Our result indicates that
383 8 iterations are a sufficient calibration budget, as the calibration progress plot in Figure S1 shows that the
384 optimization experiments almost converged in the last few iterations.

385 The computational time of one simulation is approximately 5 hours on a windows desktop with a CPU
386 Intel Core i7-4790 processing unit. However, when running 24 simulations simultaneously on the multi-core
387 platform, the computational time gets longer because of the limited cache memory resources (as discussed in Xia
388 and Shoemaker (2022a)). Cache memory is a small amount of much faster memory than main memory. The wall-
389 clock time for one iteration with 24 cores simultaneously running is about 12 hours if using the default process
390 scheduling of the nonuniform memory access (NUMA) multi-core system. We used the mixed affinity scheduling
391 proposed by Xia and Shoemaker (2022a), and the wall-clock time is reduced to about 8 hours per iteration. The
392 mixed affinity scheduling changed the default affinity setting by setting a hard affinity on the simulation of each
393 PDE model (i.e., fixing the process of each PDE simulation to one core). This approach proved to be efficient for
394 memory usage and reduced the simulation time. More details about the mixed affinity scheduling and the NUMA
395 system can be found in the study of Xia and Shoemaker (2022a). Hence, the wall-clock time of each trial takes
396 about 64 hours (8 iteration \times 8 hours/iteration).

379 **3. Numerical Results and Discussion**

380 **3.1 Comparison of Calibrating to Temperature and/or Velocity**

381 **3.1.1 Final Solutions in Goodness-of-fit Metrics**

400 We first compare the three calibration formulations in terms of goodness-of-fit metrics for both temperature and
401 velocity. Table 4 summarizes this comparison for the three formulations, i.e., i) Cali-Tem, ii) Cali-Vel and iii)
402 Cali-Both (see definition in Table 3), with PODS used as the optimization algorithm and with a budget of 192
403 simulations.

404 The mean as well as the standard deviation of both temperature error $f_{Tem}(\mathbf{X}^*|\mathbf{K})$ (calculated as Eq. (7))
405 and velocity error $f_{Vel}(\mathbf{X}^*|\mathbf{K})$ (Calculated as in Eq. (10)) over three trials are reported in Table 4, for all three
406 calibration scenarios. \mathbf{X}^* in Table 4 denotes the optimal calibration solution obtained by PODS in each trial for a
407 given scenario (defined by the set of variables \mathbf{K}). The solution with the lowest variable error ($f_{Tem}(\mathbf{X}^*)$
408 or $f_{Vel}(\mathbf{X}^*)$) is highlighted in bold in Table 4. Table 4 reports the variable errors of both temperature and velocity
409 for all formulations to understand the impact of ignoring or including a variable in the calibration formulation.

410 Please note that the temperature error, $f_{Tem}(\mathbf{X}|\mathbf{K} = [Tem])$, reported in Table 4, is exactly the calibration
 411 objective function in the Cali-Tem scenario ($F(\mathbf{X}|\mathbf{K} = [Tem])$) as shown in Eq. (7)). Similarly, the velocity error
 412 $f_{\overline{Vel}}(\mathbf{X}|\mathbf{K} = [Tem])$ is exactly the calibration objective function in the Cali-Vel scenario (i.e., $F(\mathbf{X}|\mathbf{K} = [\overline{Vel}])$)
 413 as shown in Eq. (10)). We use the word variable error instead of objective function value when referring to the
 414 values in Table 4 in subsequent discussions since we are in part looking at the impact of using data from one
 415 variable to predict another variable for which we don't have data. It is also worth mentioning that the value in
 416 Table 4 is a sum of temperature or velocity error at multiple (in total 12) locations. Hence the error at each location
 417 is smaller than the value in the table.

418 Table 4 shows that the solution obtained when calibrating to temperature observation only (Cali-Tem)
 419 has smaller temperature errors but larger velocity errors than that if calibrating to velocity observation data only
 420 (Cali-Vel). However, it is surprising that when calibrating to both temperature and velocity (Cali-Both), the
 421 solution obtained by PODS has the lowest temperature and lowest velocity error compared with calibrating to
 422 either temperature observation or velocity observation only. This might be because calibrating to temperature will
 423 help to improve the fit of velocity and vice versa. This makes sense because water temperature and velocity are
 424 two related variables in hydrodynamic modeling, and they affect each other. Velocity is the fundamental variable
 425 of hydrodynamics with directional information not provided by temperature; temperature (via the heat flux model)
 426 may also affect the velocity field since it affects water density. Our analyses here are based on physical models,
 427 which are built based on physics laws and knowledge human have learned over hundreds of years. Our findings
 428 here are in line with the study of Baracchini et al (2020), where they also suggested have both temperature and
 429 velocity for a complete system calibration.

430 **Table 4.** Summary table of the solution obtained by PODS for each scenario (Cali-Both, Cali-Vel, and Cali-Tem).
 431 $f_{Tem}(\mathbf{X}^*|\mathbf{K})$ and $f_{\overline{Vel}}(\mathbf{X}^*|\mathbf{K})$ are the temperature error $f_{Tem}(\mathbf{X}^*)$ and velocity error $f_{\overline{Vel}}(\mathbf{X}^*)$ (calculated in Eq. (7)
 432 and Eq. (10), respectively, with the optimal solution \mathbf{X}^* obtained in each trial). The mean and standard deviation
 433 of $f_{Tem}(\mathbf{X}^*|\mathbf{K})$ and $f_{\overline{Vel}}(\mathbf{X}^*|\mathbf{K})$ among three trials are reported. The variable error is bolded in each scenario when
 434 the observation of the variable is included in the calibration in each scenario. (Some terms defined in Table 1)

Scenarios	The composite error of each variable (Temperature or Velocity)	
	$f_{Tem}(\mathbf{X}^* \mathbf{K})$ Mean (Std.)	$f_{\overline{Vel}}(\mathbf{X}^* \mathbf{K})$ Mean (Std.)
Cali-Both $\mathbf{K} = [Tem, \overline{Vel}]$	0.014 (0.003)	1.939 (0.165)
Cali-Vel $\mathbf{K} = [\overline{Vel}]$	0.087 (0.023)	2.809 (0.319)
Cali-Tem $\mathbf{K} = [Tem]$	0.024 (0.005)	5.888 (1.435)

435 3.1.2 Visual Comparison of Calibration Errors

436 The above analysis is based on the average variable error statistics only (i.e., $f_{Tem}(\mathbf{X}^*|\mathbf{K})$ and $f_{\overline{Vel}}(\mathbf{X}^*|\mathbf{K})$), of the
 437 best results obtained from PODS (over multiple trials) for all calibration scenarios. In order to further analyze the
 438 difference between calibration formulations (in terms of their effectiveness in calibrating both temperature and
 439 velocity), we visually compare the best calibration solutions (\mathbf{X}^*) obtained by PODS for each scenario, i.e., Cali-
 440 Tem, Cali-Vel and Cali-Both. We select one representative optimal solution (\mathbf{X}^*) from 3 trials in each scenario
 441 for this comparison. An initial uncalibrated solution is included in the comparison. The parameter value of the
 442 uncalibrated solution (in Table S1) uses the mean of the calibration range in Table 2.

443 The objective function value in terms of temperature and velocity composite error (over multiple
 444 locations) ($f_{Tem}(\mathbf{X})$ and $f_{\overline{Vel}}(\mathbf{X})$), as formulated in Eq. (7) and (10), respectively) and the corresponding parameter

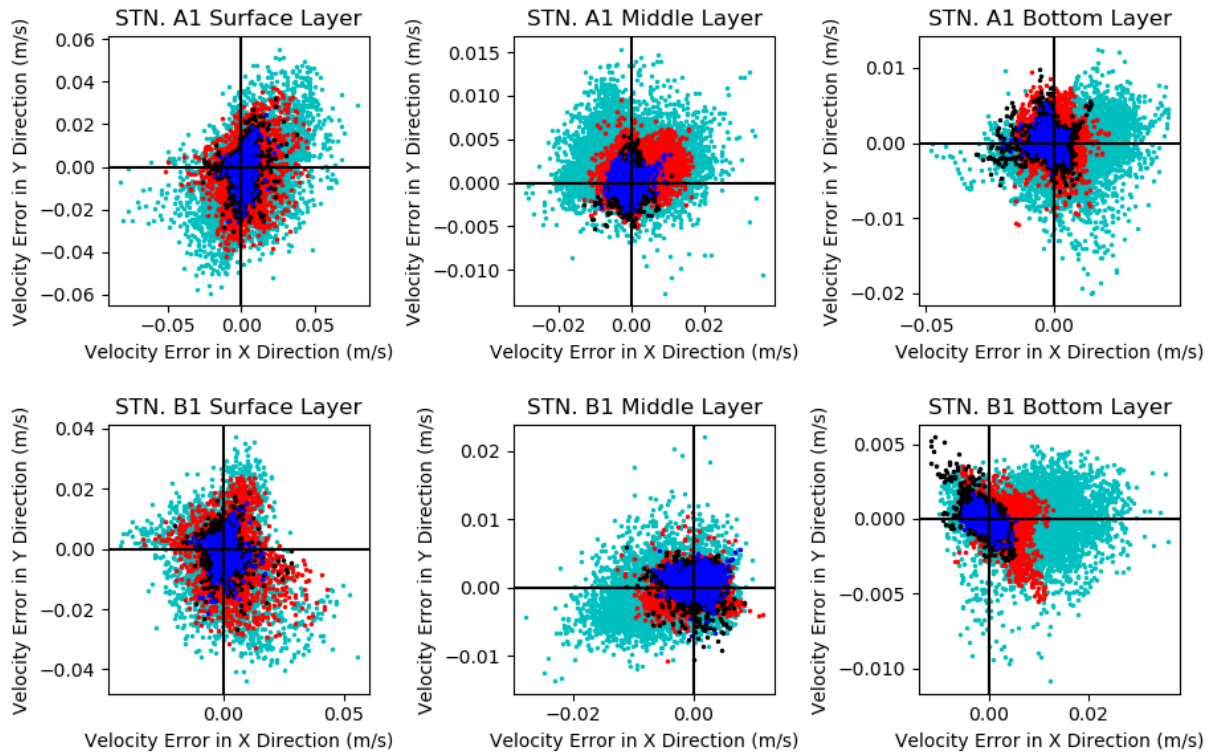
445 configuration (\mathbf{X}^*) of the selected solution (among three trials) are plotted in Fig. 5 and reported in Table S1. In
 446 general, the solution in the Cali-Both scenario is closer to the True solution than solutions in the other two
 447 scenarios in terms of parameter values. Calibrated values proposed by the Cali-Both scenario are closest (relative
 448 to other scenarios) to the True values for four parameters (i.e., D_H^{back} , D_V^{back} , H_{Secchi} , c_H). Moreover, besides the
 449 Manning coefficients, the calibrated values proposed by the Cali-Both scenario are not the worst (relative to the
 450 other two scenarios) for any other parameter. In contrast, calibrated values proposed by the Cali-Tem scenario are
 451 worst (i.e., the parameter values are farthest from the true solution, relative to other scenarios) for five parameters
 452 (i.e., v_H^{back} , D_H^{back} , v_V^{back} , D_V^{back} , c_e) and calibrated parameter values for the Cali-Vel scenarios are worst for
 453 L_{oz} , H_{Secchi} , c_H . This indicates that calibrating to both temperature and velocity can help to prevent the value of
 454 the 9 calibration parameters from being very far from the corresponding value for the True solution.

455 The horizontal velocity error $\Delta\overline{Vel}$ (2-dimensional) between simulated velocity $Sim_{t,j}^{\overline{Vel}}(\mathbf{X}^*)$ and
 456 observed velocity $Obs_{t,j}^{\overline{Vel}}$ (in the horizontal plane) is plotted as scatter plots of time-series in Fig. 3 (for all
 457 calibration scenarios). The temperature error ΔTem between simulation temperature $Sim_{t,j}^{Tem}(\mathbf{X}^*)$ and observed
 458 temperature $Obs_{t,j}^{Tem}$ is plotted as a time series (for each calibration scenario) in Fig. 4.

459 The error plots for the two sampling locations at multiple depths (i.e., surface layers of station STN. A1
 460 and STN. B1 as shown in Fig. 1 (a)) are visualized in Fig. 3 and 4 (for one year). Since the velocity error $\Delta\overline{Vel}$ at
 461 a particular time and location is a vector (and not a scalar like temperature) and velocity error in 3 dimensions (for
 462 a time-series) is hard to represent visually, Fig. 3 only plots the velocity error (for one year) $\Delta\overline{Vel}$ in the horizontal
 463 plane (i.e., X and Y directions only). Moreover, each dot represents the error at one point in time within the study
 464 period.

465 Figure 3 plots the difference between the simulated velocity (for the optimized parameter values obtained
 466 from Cali-Tem (red scatter points), Cali-Vel (black scatter points), and Cali-Both (blue scatter points) scenarios)
 467 and observed velocity. Ideally, the error for each scatter point should be zero, i.e., at the intersection of the two
 468 lines. Figure 3 illustrates that calibrating to temperature data only (red scatter plot) results in a larger velocity
 469 error $\Delta\overline{Vel}$, relative to velocity error when calibrating to velocity data only (Cali-Vel scenario, i.e., black scatter
 470 plot) or to both velocity and temperature data (Cali-Both scenario, i.e., blue scatter plot). Figure 3 also shows that
 471 solutions of all the three scenarios improved the temperature fit compared with the initial solution, which
 472 demonstrates the effectiveness of the optimization calibration.

473



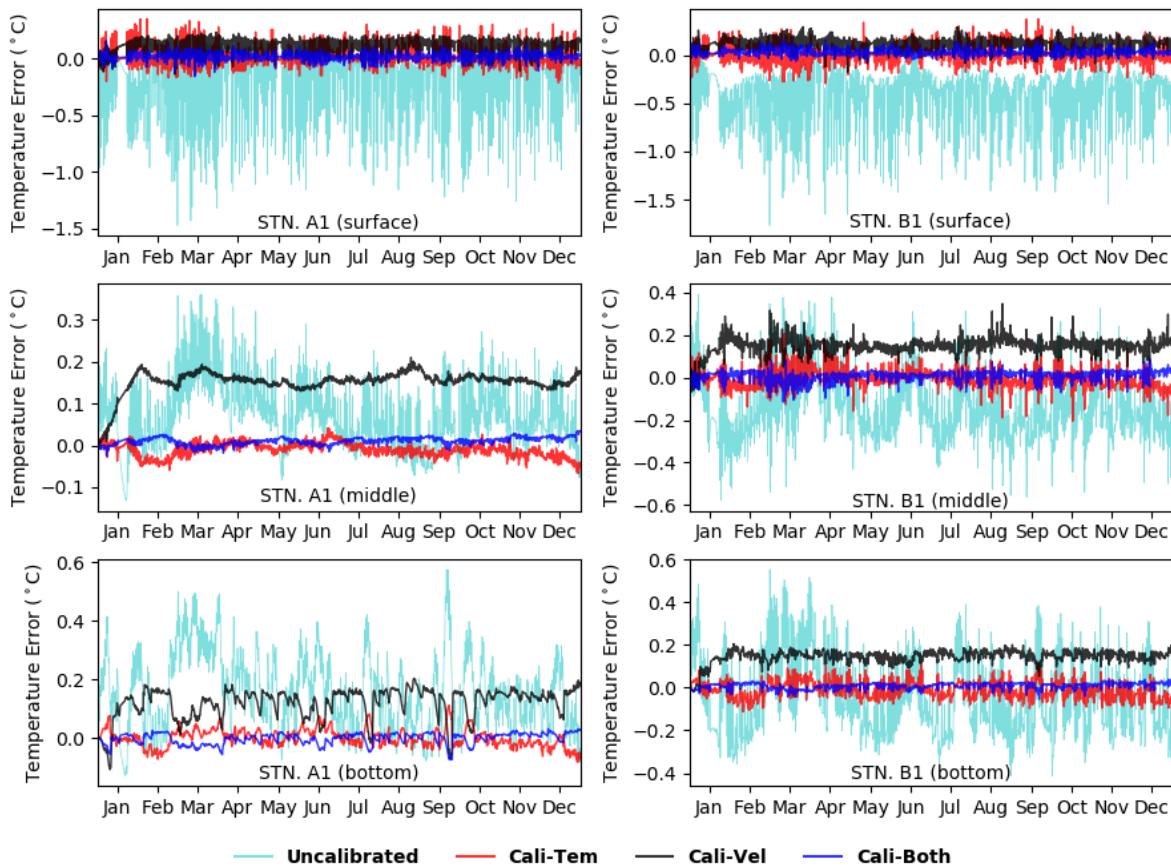
474
475

476 **Figure 3.** Scatter plot of velocity error $\Delta \vec{vel}$ in horizontal (X and Y direction) between simulated velocity
 477 $Sim_{t,j}^{\vec{vel}}(\mathbf{X}^*)$ and observed velocity $Obs_{t,j}^{\vec{vel}}$ at location j . Each dot denotes the velocity error $\Delta \vec{vel}$ of location j at
 478 one time step. j = surface layer of STN. A1 for upper panel and j = STN. B1 for lower panel. \mathbf{X}^* is the optimal
 479 solution found by PODS in each scenario: Cali-Tem (red dots); Cali-Vel (black dots) and Cali-Both (blue dots)
 480 as listed in Table S1. The “True” solution is on or near the intersection of the two perpendicular black lines. An
 481 initial uncalibrated solution (cyan dots) is plotted for reference.

482 Figure 4 shows the temperature error of solutions from three different calibration scenarios: Cali-Tem
 483 (red time-series), Cali-Vel (black time-series) and Cali-Both scenarios (blue time-series). The errors between
 484 simulated and observed water temperature at the surface, middle and bottom layers of two stations (STN. A1 and
 485 STN B1) are plotted. In general, the temperature error of the solution in Cali-Both scenario is generally close to
 486 zero °C for all the layers and stations shown. The solution in Cali-Tem scenario also got temperature errors close
 487 to zero °C at the middle and bottom layer at STN. A1, but it has larger temperature errors than the solution in the
 488 Cali-Both at the surface layer of STN. A1 and all layers of STN. B1. The solution in the Cali-Vel scenario
 489 generally overestimated the water temperature in all locations (i.e., all the surface, middle and bottom layers at
 490 both stations). The temperature error of the solution in the Cali-Vel scenario is much larger than that of the solution
 491 in Cali-Tem and Cali-Both scenarios in the middle and bottom layers of both stations. The temperature error at
 492 most times, for the Cali-Vel scenario, is greater than 0.1 °C. This might be because both the Stanton and Dalton
 493 numbers are underestimated in the Cali-Vel scenario when compared with the True solution (\mathbf{X}^R) (As shown in
 494 Fig. 5). The Dalton number C_e affects the evaporative heat flux modeling and the Stanton number C_H influences
 495 the convective heat flux modeling in the Delft3D-FLOW model (Hydraulics, 2006). For the solution in Cali-Vel,
 496 a smaller Stanton number C_H (shown in Fig. 5) might lead to underestimated convective heat flux, which will lead
 497 to the overestimation of the water temperature. In summary, calibrating to temperature and velocity (i.e., Cali-
 498 Both) give the best solution in terms of temperature error compared with calibrating to temperature or velocity
 499 only (i.e., Cali-Tem or Cali-Vel). Calibrating to velocity only (Cali-Vel) gives the worst result in terms of

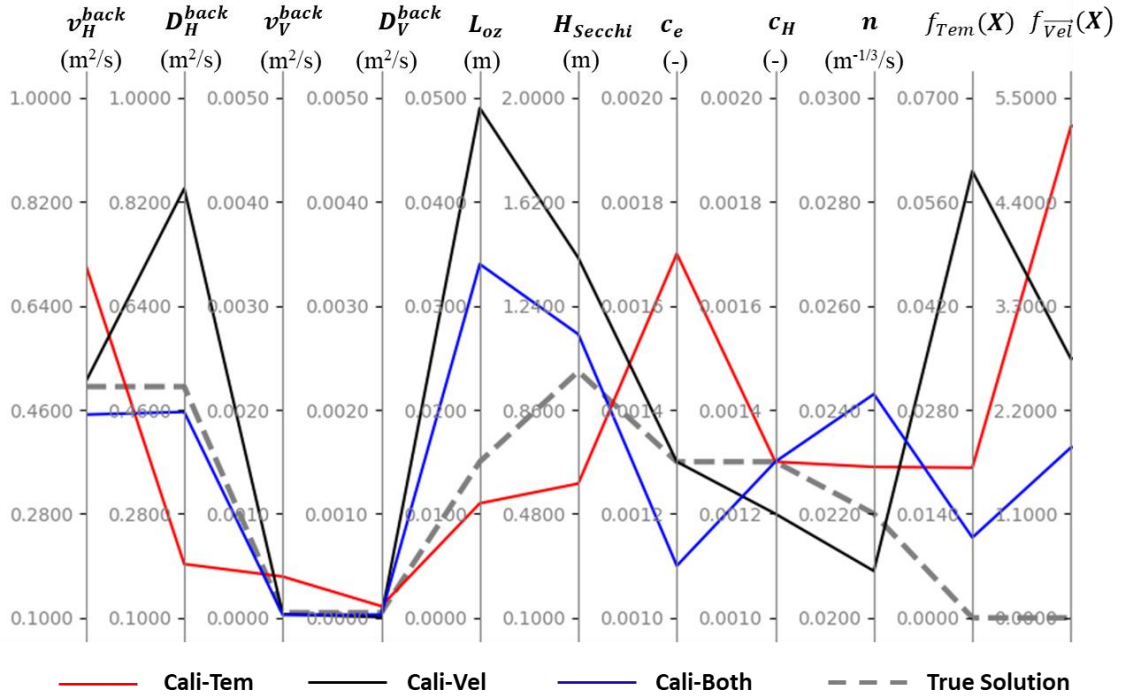
500 temperature fit. Simulation of vertical temperature, vertical velocity, vertical eddy diffusivity, and vertical eddy
 501 viscosity (Fig. S2-S5) also shows that the solution in the Cali-Both scenario is much better than solutions in the
 502 Cali-Tem and Cali-Vel scenario. For example, the solution in the Cali-Both scenario can almost capture the
 503 vertical time-varying temperature profiles of the true solution. In contrast, calibrating to one variable did not fully
 504 capture the vertical time-varying temperature profiles (e.g., April-May for the Cali-Tem scenario; Mar-May and
 505 Aug-Sep for the Cali-Both scenario in Fig. S2.) The solution in the Cali-Both scenario also gives much smaller
 506 vertical velocity, eddy diffusivity, and eddy viscosity error than solutions in the other two scenarios (in Fig. S3-
 507 S5). The result indicates that using both temperature and velocity data in model calibration also helps to improve
 508 the complex time-varying vertical mixing behavior.

509



510

511 **Figure 4.** Time-series plots of temperature error ΔT between simulated water temperature and $Sim_{t,j}^{Tem}(X^*)$ and
 512 observed water temperature ($Obs_{t,j}^{Tem}$) at location j where $j =$ surface layer of STN4 for left panel and $j =$ STN1
 513 for the right panel. X^* is the optimal solution found by P-DYCORs in each scenario: Cali-Tem (Red lines); Cali-
 514 Vel (Black lines) and Cali-Both (blue lines) as listed in Table S1. An initial uncalibrated solution (cyan lines) is
 515 plotted for reference.



516

517 **Figure 5.** The parallel axis plot for the parameter value and the composite error of temperature and velocity of
518 calibration solutions under different scenarios (Cali-Tem, Cali-Vel, and Cali-Both). True solution defined in Table
519 2 is given for reference. Smaller variable errors ($f_{Tem}(X)$ (see Eq. (7)) and $f_{Vel}(X)$ (see Eq. (10))) are better, and
520 the variable errors of the true solution (X^R) are zero (for both $f_{Tem}(X)$ and $f_{Vel}(X)$). The parameter symbols are
521 defined in Table 2.

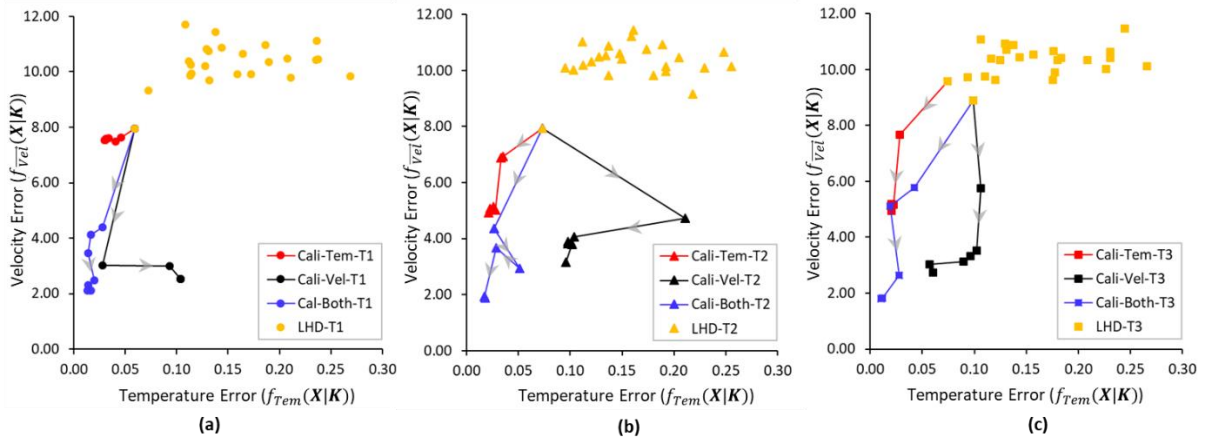
522 3.2 Optimization Search Dynamics under Different Calibration Scenarios

523 We further analyze the calibration progress of PODS for Cali-Tem, Cali-Vel and Cali-Both, to understand the
524 calibration convergence speeds of the three formulations. The purpose of the calibration progress analysis is to
525 visualize the improvement in calibration quality of both temperature and velocity variables from the LHD, for all
526 three formulations. As discussed in the experiment setup section, we conducted 8 iterations of the optimization
527 search. This is a reasonable number of iterations for our case, given that 1) the problem is computationally
528 expensive (one experiment takes about 64 hours to run and there are 9 experiments) and 2) the calibration progress
529 plot in iterations (Figure S1) indicates that the optimization search almost converged in 8 iterations.

530 Figure 6 plots the calibration progress of the three formulations (i.e., Cali-Tem, Cali-Vel and Cali-Both)
531 using PODS. Each subplot within Fig. 6, corresponds to the different concurrent optimization trials (i.e., trials of
532 the stochastic optimization method using the same initial points from LHD) for each formulation. The best
533 solutions are near the origin of each graph. Moreover, Fig. 6 plots the progress (quantified by visualizing both
534 temperature and velocity errors) of the best solution found (measured in terms of the objective function value in
535 each calibration scenario) during the search. Figure 6 indicates that when calibrating to temperature or velocity
536 only, the optimization search cannot guarantee the improvement of the fit of another variable. For example, in
537 Fig. 6 (a), when calibrating to velocity only, the temperature error of the best solution found at the end of the
538 optimization search stage is worse than the temperature error of the best solution found after the initial LHD, even
539 though there is improvement in terms of velocity fit. Similarly, when calibrating to temperature only, the
540 improvement in velocity fit is also not significant (for instance, in Fig. 6 (a)). When calibrating to the fit of both

541 temperature and velocity using the DYNO formulation, the fit of both temperature and velocity improves in all
 542 trials, and the improvement remains balanced during the optimization search. Figure 6 also indicates that the final
 543 solution found in Cali-Both scenarios dominates the best solution found by PODS in Cali-Tem and Cali-Vel in
 544 terms of both temperature and velocity fit.

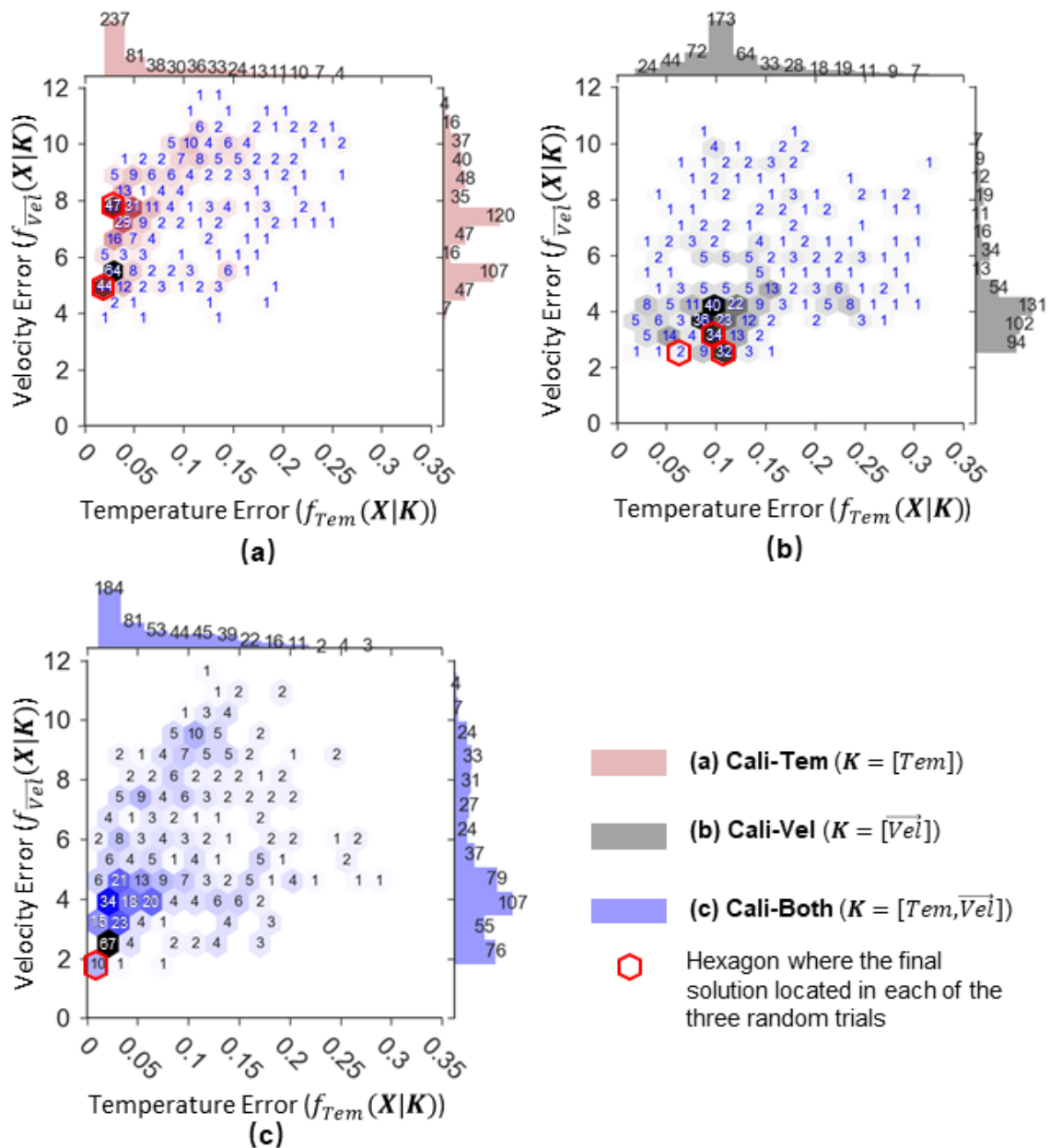
545 Figure 6 also shows that when calibrating to one variable, the optimization search is easily convergent
 546 (i.e., the best solution does not continue improving after a few iterations even in terms of the fit of the variable
 547 considered in calibration). For example, in Fig. 6(a), when calibrating to temperature only, the best solution in
 548 terms of temperature error does not improve much (in the last few iterations). The reason might be that when the
 549 velocity error is large, it is less likely that the temperature fit would be improved further. In contrast, when
 550 calibrating to both temperature and velocity, the optimization search continues improving in both the temperature
 551 and velocity fit. Hence only considering one variable in the calibration, it is difficult to get a solution that has
 552 small (or close to zero) errors of the variable considered. We should also highlight that even though the
 553 optimization gets a solution that has zero error in one variable, it does not mean that the error of another variable
 554 would be zero. The reason is that only the observation in part of the simulation space is used for calibration (not
 555 the observation data at each grid and each time step of the simulation space are used to calculate the temperature
 556 error). So the temperature error may be 0 at these observation locations, while the temperature error is not 0 at
 557 other locations where observation is not used in calibration. In this case, getting a temperature error 0 at
 558 observation locations cannot guarantee the velocity error is 0.



559 **Figure 6.** Calibration progress plot of the best solution found (in terms of objective function value) during
 560 optimization search by PODS when calibrating to temperature only (Cali-Tem), calibrating to velocity only (Cali-
 561 Vel), and calibrating to both temperature and velocity (Cali-Both). Three random trials (i.e., T1, T2, and T3) are
 562 plotted in (a), (b), and (c). Lower velocity and temperature error are better. The yellow makers are evaluation
 563 point in initial experiment design using LHD. Besides solutions in LHD, only the best solution in each of the
 564 optimization iterations is plotted (i.e., makers lined with lines). The line links the best previous solution in one
 565 iteration to the best solution in next iteration. The arrow indicates the direction from the previous solution to the
 566 next solution.

567 It is also important to understand the ‘frequency’ or likelihood with which PODS can find good
 568 temperature and velocity calibrations via the three different formulations proposed in this study. Hence, we also
 569 do a comparative frequency analysis of the errors (for velocity or temperature) of all evaluated points ($X_i, i =$
 570 $1, \dots, 3 \times N_{max}$) from all trials (3 trials) of PODS when using different calibration formulations (see Table 3). The
 571 purpose of this frequency analysis is to understand the likelihood with which the three different formulations can
 572 obtain good velocity and temperature calibrations. The frequency analysis results are presented in Fig. 7 via
 573

574 visualizations of empirical histograms of both velocity error and temperature error (from all solutions of 3 trials
 575 of PODS) for each calibration scenario.



576 **Figure 7.** Distribution plot of all the evaluated points found by PODS (over 3 trials) in terms of temperature
 577 composite error $f_{Tem}(\mathbf{X}|\mathbf{K})$ and velocity composite error $f_{\overline{Vel}}(\mathbf{X}|\mathbf{K})$ in each scenario: Cali-Tem ($\mathbf{K} = [Tem]$),
 578 Cali-Vel ($\mathbf{K} = [\overline{Vel}]$), and Cali-Both ($\mathbf{K} = [Tem, \overline{Vel}]$). The number inside each hexagon represent the number
 579 of evaluated points located in that hexagon (e.g. with the combination temperature and velocity error associated
 580 with the corresponding values on the axes.) Darker color in hexagon means larger number of evaluated points is
 581 located in that hexagon. The bar plot along the upper x axis ($f_{Tem}(\mathbf{X}|\mathbf{K})$) are the distribution of the evaluation
 582 points in terms of temperature error only. The bar plot along y axis ($f_{\overline{Vel}}(\mathbf{X}|\mathbf{K})$) are the distribution of the
 583 evaluation points in terms of velocity error only. The number above the bar shows how many evaluated points
 584 located in that bin. Smaller error ($f_{Tem}(\mathbf{X}|\mathbf{K})$ or $f_{\overline{Vel}}(\mathbf{X}|\mathbf{K})$) is better. The true solution ($f_{Tem}(\mathbf{X}^R|\mathbf{K}), f_{\overline{Vel}}(\mathbf{X}^R|\mathbf{K})$)
 585 is the origin of each subplot.

587 Figure 7 plots the error distribution of all the evaluated points over three trials (576 evaluations) for each
 588 scenario: Cali-Tem ($\mathbf{K} = [Tem]$), Cali-Vel ($\mathbf{K} = [\overline{Vel}]$), and Cali-Both ($\mathbf{K} = [Tem, \overline{Vel}]$). The different subplots
 589 in Fig. 7 provide a visualization of the velocity (vertical axis) and temperature (horizontal axis) error distribution

590 via hexagonal bin (hexbin) plots (inside the square) and error histograms (outside the square) for each of the
 591 calibration scenarios. The number inside each hexbin denotes the number of evaluated points (for that combination
 592 of temperature error and velocity error) located in that hexbin. Furthermore, the hexbin with a larger number of
 593 evaluated points is highlighted with a darker color shade. The temperature histogram columns (above the square)
 594 represent the sum of all the hexbins inside the square directly beneath the number in the column. For the velocity
 595 histogram (on the right side of square), the column height depends on the sum of all the hexbins in the row to the
 596 left of the number.

597 The temperature and error velocity distribution visualizations of Fig. 7 clearly show that calibrating to
 598 both temperature and velocity data (see Fig. 7 (c), i.e., error distribution for the Cali-Both scenario), provides good
 599 temperature and velocity calibrations with a higher frequency. Figure 7 (c) shows that it is highly likely that both
 600 temperature and velocity errors are lower (indicated by darker hexbins with temperature error $f_{Tem}(\mathbf{X}|\mathbf{K})$ less
 601 than 0.05 and velocity error $f_{vel}(\mathbf{X}|\mathbf{K})$ less than 4). Consequently, Fig. 7(c) also illustrates that the newly
 602 proposed DYNO (see Eq. (3)) works effectively, in this case, to calibrate multiple variables simultaneously.

603 Figure 7 also illustrates that it is better to calibrate the hypothetical hydrodynamic model to velocity data
 604 rather than temperature data (see Fig. 7(a) and Fig. 7(b)) (if data for both variables is not available). Figure 7(a)
 605 indicates that calibrating to temperature only (i.e., the Cali-Tem scenario) results in a high chance that velocity
 606 error would be high (see the velocity error histogram in Fig. 7(a)). However, Fig. 7(b) illustrates that the errors in
 607 temperature when calibrating to velocity only (Cali-Vel) are likely to be relatively small in magnitude (see the
 608 temperature error histogram of Fig. 7(b)).

609 From the above discussion, we can conclude that calibrating to both temperature and velocity data with
 610 the newly proposed DYNO (implemented within the efficient surrogate algorithm PODS) is effective in obtaining
 611 a balanced calibration of both temperature and velocity variables. In real-world lake hydrodynamic applications,
 612 if available, both temperature and velocity data should be used for lake hydrodynamic model calibration.
 613 However, the very common practice of calibrating only to temperature data is shown to be unable to reproduce
 614 the flow dynamics well. This supports the extra effort and expense to collect velocity data is expected to give a
 615 beneficial effect.

616 3.3 Impact of Different Forms of Normalization on the Performance of DYNO

617 This section investigates the impact of using different forms of normalization in the new objective function DYNO
 618 on optimization search performance. In Eq. (3), the error of each variable is normalized by the maximum and
 619 minimum values $f_k^{max}(\mathbf{X})$ and $f_k^{min}(\mathbf{X})$ of $f_k(\mathbf{X})$ among all the evaluations evaluated so far. One concern of
 620 using the maximum value $f_k^{max}(\mathbf{X})$ is that the objective function can be affected by extremely bad evaluation
 621 points. Another approach is to use the median value $f_k^{median}(\mathbf{X})$ of $f_k(\mathbf{X})$ among all the evaluations evaluated so
 622 far as a replacement of $f_k^{max}(\mathbf{X})$ to normalize the error of each variable. We refer to DYNO using the median
 623 value $f_k^{median}(\mathbf{X})$ as DYNO-N2 (as shown in Eq. (13)) to differentiate it from DYNO using the maximum value
 624 $f_k^{max}(\mathbf{X})$ (as shown in Eq. (3)), which we refer to as DYNO-N1 in the following text.

$$625 F(\mathbf{X}|\mathbf{K}) = \sum_{k \in \mathbf{K}} \frac{f_k(\mathbf{X}) - f_k^{min}(\mathbf{X})}{f_k^{median}(\mathbf{X}) - f_k^{min}(\mathbf{X})} \quad (13)$$

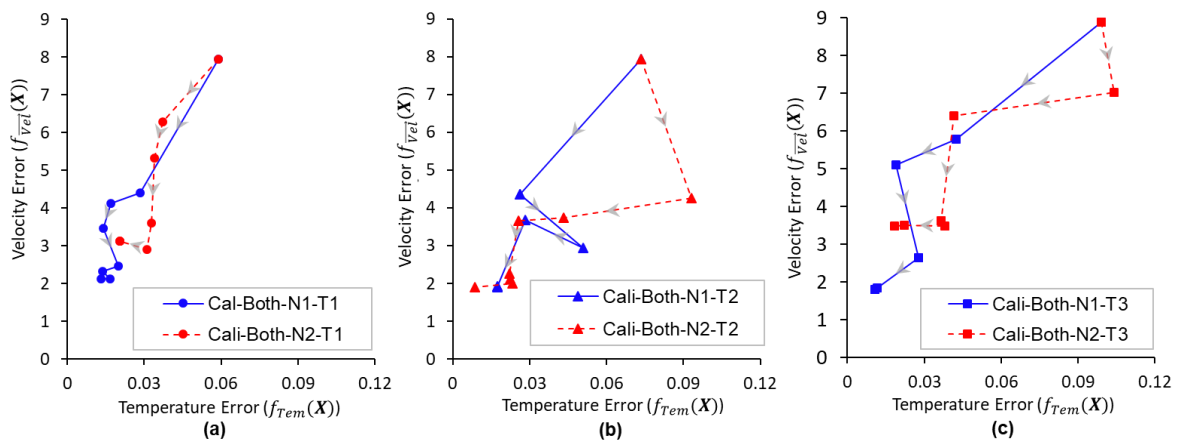
$$626 f_k^{median}(\mathbf{X}) = \text{med}\{f_k(\mathbf{X}) \text{ for all } \mathbf{X} \in \psi\} \quad (14)$$

627

628 where $f_k^{median}(\mathbf{X})$ and $f_k^{min}(\mathbf{X})$ are the median and minimum values of $f_k(\mathbf{X})$ among all the evaluations
 629 evaluated so far, and hence they are updated dynamically in each iteration during optimization.

630 The implementation of DYNO-N2 is similar to the implementation of DYNO-N1 (Eq. (3)). The only
 631 change is replacing the calculation related to $f_k^{max}(\mathbf{X})$ with $f_k^{median}(\mathbf{X})$. We tested the relative efficacies of
 632 DYNO-N1 and DYNO-N2, by comparing three calibration trials, of each DYNO variant (using PODS), where
 633 each concurrent calibration trial was initialized using the same LHD. Figure 8 shows the progress of PODS with
 634 the two forms of DYNO as the objective functions. Figure 8 is similar in design to Fig. 6, and indicates that both
 635 forms of DYNO are able to balance the calibration on temperature and velocity. There are two trials where PODS
 636 with DYNO-N1 (using $f_k^{max}(\mathbf{X})$ for normalization) found a better solution than PODS with DYNO-N2 (using
 637 $f_k^{median}(\mathbf{X})$ for normalization).

638 The results here indicate that DYNO-N1 seems not adversely affected by the bad solution. A reason for
 639 this may be that PODS typically do not generate extremely bad solutions (i.e., outlier solutions with extremely
 640 large errors), since algorithm search is concentrated around the best solution found so far. However, if other
 641 optimization algorithms are used for calibration, especially algorithms that explore the search space more, there
 642 might be a higher likelihood of encountering outlier /extremely bad solutions during optimization search.
 643 Consequently, the performance of such an algorithm with DYNO-N2 might be better than with DYNO-N1, which
 644 might need further investigation. The outlier solutions here mean solutions (obtained during the optimization
 645 search phrase) that have much larger errors than other solutions found so far. Outlier or extremely bad solutions
 646 are also likely to happen for calibration problems where the model output is very sensitive to the calibration
 647 parameters (i.e., a small change in model parameters can cause huge changes in the model output that leads to
 648 much worse solutions).



649 **Figure 8.** Calibration progress plot in terms of the best solution found during optimization search when using
 650 DYNO-N1 and DYNO-N2 as the objective function. Three random trials (T1, T2, and T3) are plotted in (a), (b),
 651 and (c). Lower velocity and temperature error are better. Figure 8 uses the same format as Figure 6.

653 3.4 Value of Velocity Measures in 3D Lake Model Calibration

654 High quality hydrodynamic simulations (e.g., thermal structure, current velocities, flow advection and vertical
 655 mixing) are vital for accurate spatial modelling of water quality in lakes. The hydrodynamic process influences
 656 the transport & production or transformation of biological and chemical components. Hence, if the simulation of
 657 flow dynamics is not adequately accurate, there is no way to achieve accuracy in the simulation of water quality.

658 Previous studies use mostly temperature observations for the 3D lake hydrodynamic model calibration. Whereas,
659 velocity data is less commonly used compared with temperature data for model calibration.

660 Our results in section 3.1 indicate that calibrating to temperature data only cannot guarantee accuracy in
661 velocity simulation in our case. Not using velocity data in model calibration (i.e., using temperature data in model
662 calibration only) thus, may lead to large velocity errors (as indicated in the Fig. 3). The inclusion of velocity
663 measurements in calibration not only reduces velocity error but also helps **improve** the temperature fit. For
664 example, in Fig. 4, when calibrating to both temperature and velocity data, the temperature error is smaller than
665 the temperature error when calibrating to temperature data only. This is most obvious in the surface layers of both
666 STN. A1 and STN. B1, where the temperature error when calibrating to both temperature and velocity (i.e., Cali-
667 Both) is much smaller compared to calibrating to temperature only (i.e., Cali-Vel). The better result (better fit of
668 temperature as well as velocity) in Cali-Both demonstrates the effectiveness of using velocity measures in 3D
669 hydrodynamic lake model calibration. The comparison of calibrated parameter values in Cali-Both and Cali-Tem
670 scenarios (in Fig. 5) also demonstrates the value of using velocity data besides temperature data in model
671 calibration. In Fig. 5, we can see that the calibrated value of viscosity and diffusivity parameters in Cali-Both is
672 much closer to the true value than that in Cali-Tem. This shows that the use of velocity measures helps to improve
673 the calibration of these viscosity and diffusivity parameters. Our analysis is based on synthetic observation data
674 from the physical model since we **do not** have real velocity measurements. These physical models are based on
675 physics laws. The analysis from modelling can provide some implications for the real-world situation. Hence, it
676 is worthwhile to repeat the analysis based on real data if there are real velocity measurements available in **the**
677 future.

678 The risk of using only temperature data without velocity data, even for accurately simulating water
679 temperature, is that temperature simulation is affected by both the flow dynamics and the heat transfer process.
680 The fit of temperature data is a result of the combination of these two processes. However, the fit of the
681 temperature data cannot guarantee accurate simulation of each of the processes, though accurate simulation of
682 each process does guarantee the fit of temperature data. The velocity observation hence is valuable to help improve
683 the flow dynamics simulation of the model, which is not only important for temperature simulation but also for
684 other water quality substances simulation (e.g., biological and chemical components). Our research implication
685 of the use of velocity observations is also in line with the study of Baracchini et al. (2020), where they also suggest
686 having both temperature and current velocity for complete system calibration.

687 **3.5 Possibilities for Other Applications**

688 In this study, we only demonstrate how DYNO can be incorporated into PODS parallel surrogate global
689 optimization algorithm. (see section 2.6). However, the new objective function DYNO could also be easily
690 utilized with other heuristic optimization methods (e.g., serial or parallel versions of Genetic Algorithm (Davis,
691 1991) and Differential Evolution (Tasoulis et al., 2004)) for effectively calibrating other multi-variable calibration
692 problems. We have not provided a precise methodology for incorporating DYNO into other optimization methods
693 though, since **the** incorporation of DYNO depends on the structure of an optimization method, and structures of
694 optimization methods vary a lot. We did illustrate in section 2.6 and Figure 3 on how components of parallel
695 PODS are modified in order to use DYNO. Other optimization methods could be modified in a similar way to
696 incorporate DYNO for use in multi-variable calibration.

697 Also, there are numerous other model calibration paradigms in general hydrology and water resources
698 (besides the hydrodynamic model calibration) where simultaneous multi-variable and multi-site calibrations are
699 required. Some examples of such multi-variable & multi-site calibration problems include watershed model
700 calibration (Franco et al., 2020; Odusanya et al., 2019), and seawater intrusion model calibration (Coulon et al.,
701 2021), and water quality model calibration (Xia and Shoemaker, 2021; Xia and Shoemaker, 2022b) etc. In these
702 problems, there are usually multiple constituents (e.g., substances) to be calibrated and the observations are
703 usually available at multiple locations. Our new DYNO can potentially be used to calibrate them simultaneously.
704 A popular calibration strategy for such problems in general hydrology is to use multi-objective calibration where
705 it is assumed that a trade-off exists between multiple hydrologic responses (e.g., high flow, low flow, water
706 balance, water quality etc.)

707 Using multi-objective algorithms, however, for calibrating hydrologic and watershed quality models may
708 not be the most suited strategy for some case studies because i) multi-objective calibration can be computationally
709 intensive if underlying simulations are computationally expensive and ii) meaningful trade-offs between different
710 objectives may not exist. Kollat et al. (2012) demonstrate that prior multi-objective calibration exercises may have
711 over-reported the number of meaningful trade-offs in hydrologic model calibration. DYNO is a reasonable
712 alternative to classical multi-objective calibration in calibration problems where the trade-off between multiple
713 component calibration objectives is not significant, because i) a balance between multiple constituent objectives
714 is maintained with DYNO and ii) a single objective algorithm can be used with DYNO, which is computationally
715 more efficient than a multi-objective algorithm. This is especially true for multi-constituent watershed model
716 calibration problems where the achievable objective functions ranges for different constituents (e.g., flow,
717 sediment, phosphorus etc.) are quite different. Multiple prior studies (Moriassi et al., 2012; Moriassi et al., 2015)
718 highlight that achievable ranges of statistical calibration measures (e.g., Nash Sutcliffe Efficiency (NSE), bias
719 etc.) are significantly different for different constituents (e.g., streamflow, sediment, total phosphorus etc.).
720 Moriassi et al. (2015) note that in most watershed model case studies, the achievable range of NSE for streamflow
721 is higher than the achievable range for total phosphorus. Hence, DYNO may be extremely effective in balancing
722 simultaneous calibration of streamflow and phosphorus for such case studies. We believe that there is immense
723 potential in the application of DYNO for multi-constituent watershed model calibration.

724 DYNO is also applicable to multi-constituent calibration problems where sampling locations and
725 temporal frequencies for the different constituents are different. For instance, in real world hydrodynamic settings,
726 it is very likely that sampling locations and frequencies of temperature and velocity observations are different.
727 This is also true for watershed sampling settings, where sampling locations and frequencies for water quality (e.g.,
728 phosphorus) constituents are, typically, less than sampling distributions of streamflow. While the synthetic
729 experiments of this study assume identical sampling locations & frequencies for temperature and velocity, DYNO
730 requires the observations of multiple constituents (e.g., temperature and velocity in our case). It **is worth**
731 mentioning that DYNO does not require the same number of locations or same time frequency for different
732 observation constituents. This is because DYNO first calculates the composite error of each constituent separately
733 and then normalizes the composite error of each constituent dynamically, to balance the calibration of each
734 constituent. This feature of DYNO allows it to be used in cases where different constituents are measured in
735 different locations or time frequencies.

736 3.6 Future Work

737 Our analysis of the role of temperature and velocity measurements in 3D hydrodynamic model calibration is based
738 on synthetic observation data generated from models. We do think it is worthwhile to further investigate the role
739 of temperature and velocity measurements in hydrodynamic model calibration if there are velocity measurements
740 available in the future. Moreover, the synthetic observation data used in our analysis did not account for the
741 measurement uncertainty of observation data. Further investigations related to the impact of measurement errors
742 on the calibration setup proposed here will also be beneficial. It is important to note that the measurement
743 uncertainty and distribution of different variables could be different (and thus, our new objective function
744 formulation DYNO could be very useful in balancing the calibration process in such a scenario). For example,
745 Baracchini et al. (2020) reported that the measured and computed velocity value (in the magnitude of 1 cm s^{-1} for
746 velocity in hypolimnion layer) is close to velocity measurement uncertainty 0.8 cm s^{-1} (the velocity measurement
747 instrument precision) while the computed and measured temperature value is an order of magnitudes larger
748 relative to temperature measurement uncertainty in their study. The difference in terms of measurement accuracy
749 and measurement value could lead to a different magnitude of error function value for each variable (temperature
750 or velocity). (In their study, the error function is the square of temperature (or velocity) difference between
751 computed and measured value divided by the observational uncertainty). Baracchini et al. (2020) pointed out that
752 such discrepancy hinders the use of different kinds of data (e.g., temperature and velocity) simultaneously because
753 the impact of velocity on the cost function is almost negligible compared with temperature observations. Hence,
754 they carried out a separate discussion for both types of observation data. Their argument is true if the calibration
755 objective function is a sum of temperature or velocity's error function with a fixed weight. In this case, the
756 difference of the error function value's magnitude might lead to a biased calibration to the variable that has a
757 larger impact on the error function.

758 However, our proposed new objective function DYNO dynamically normalizes the error function value
759 of each variable using the maximum and minimum value of each variable's error function value obtained during
760 the calibration and hence balances the impact of each variable on the objection function. Hence DYNO is designed
761 to work well in scenarios where the error function values of each variable are significantly different due to
762 differences in measurement uncertainty and the distribution of each variable's observations.

763 Another possible future work is the consideration of the spatial-temporal variability of calibration
764 parameters (such as Secchi depth, Ozmidov length scale, Dalton number, and Stanton number). We considered
765 them as constant parameters in our study to simplify the problem. This is reasonable since our study area is
766 relatively small and there is not much seasonal variation. In cases where the study areas are large and there is
767 significant seasonal variation, there might be a need to consider these parameters as space and time-varying
768 calibration parameters. The consideration of space and time variability will, of course, increase the number of
769 decision variables for the optimization problems, which will bring more challenges. In that case, new methods on
770 how to reduce the parameter dimensions might be needed (e.g., designing some low dimensional controlling
771 parameters, like curve number in hydrology (Bartlett et al., 2016), to represent the high dimensional space-time
772 variability of these parameters).

773 **4 Conclusions**

774 We conclude that the DYNO objective function that we propose is a new effective way to balance the calibration
775 to different variables (i.e., temperature and velocity) in optimization-based -calibration. It is possible that the
776 magnitudes of goodness-of-fit measures for different variables are very different (which may fluctuate during the
777 optimization search), and thus the optimization search cannot maintain **the** balance between different variables.
778 Hence DYNO dynamically modifies the objective function, for multi-variable calibration, so that the error for
779 each variable **is dynamically** normalized in each iteration. This is to ensure that the search is giving approximately
780 equal weight to each variable (e.g., velocity and temperature).

781 The proposed DYNO is tested in this study for simultaneous temperature and velocity calibration of a
782 lake model. Moreover, DYNO is integrated with the PODS algorithm for testing on expensive lake hydrodynamic
783 model calibration in parallel. Results indicate that using DYNO ensures a balanced calibration between
784 temperature and velocity. We provide a detailed analysis to illustrate that DYNO balances the weight between
785 different objectives dynamically, and thus allows for a balanced parameter search during optimization.

786 We conclude that calibrating to the error of one variable (either temperature or velocity) cannot guarantee
787 the goodness-of-fit of another variable in our case. Of course, the most accurate predictions can be obtained by
788 having both temperature and velocity data. These comparisons are possible because we have, via synthetic
789 simulation, the true solution for the lake model. Our analysis suggests that for practical applications, both
790 temperature and velocity data might need to be considered for model calibration. The common practice of
791 calibrating only to temperature data might not be sufficient to reproduce the flow dynamics accurately and extra
792 effort and expense to collect velocity data is expected to give a beneficial effect. However, our analysis is based
793 on synthetic data from models, hence it is worthwhile to further investigate the role of temperature and velocity
794 in model calibration with real temperature and velocity measurements.

795 There are many possible future areas for **the** application of this method. DYNO would be effective for
796 other multi-variable and multi-site calibration problems (especially for problems with many variables). Future
797 research could apply the DYNO methods **to** other problems and **use** other optimization algorithms.

798 **Code and Data availability**

799 The tropical reservoir hydrodynamic numerical model and data were provided by PUB, Singapore's National
800 Water Agency (<https://www.pub.gov.sg/>). The Delft3D open source code could be downloaded from
801 <https://oss.deltares.nl/web/delft3d/source-code>. The PODS open source code could be download from
802 <https://github.com/louisXW/PODS>. The code for objective function can be download from
803 <https://github.com/louisXW/DYNO-pods>.

804 **Author contributions**

805 WX took responsibility for the methodology, software, formal analysis, investigation, original draft preparation,
806 and visualization. WX, TA, CAS discussed the design and results and edited the manuscript.

807 **Competing interests**

808 The authors declare that they have no conflict of interest.

809 Acknowledgments

810 This research was supported by the National Research Foundation, Prime Minister's Office, Singapore under its
811 Campus for Research Excellence and Technological Enterprise (CREATE) programme and from Professor
812 Shoemaker's start-up grant from the National University of Singapore (NUS). The authors acknowledge PUB,
813 Singapore's National Water Agency for providing the tropical reservoir hydrodynamic numerical model and data.
814 The computational work for this article was entirely performed on resources of the National Supercomputing
815 Centre, Singapore (<https://www.nscg.sg>).

816 References

- 817 Afshar, A., Kazemi, H., and Saadatpour, M.: Particle swarm optimization for automatic calibration of large scale
818 water quality model (CE-QUAL-W2): Application to Karkheh Reservoir, Iran, *Water Resources*
819 *Management*, 25, 2613-2632, 2011.
- 820 Afshar, A., Shojaei, N., and Sagharjooghifarahani, M.: Multiobjective calibration of reservoir water quality
821 modeling using multiobjective particle swarm optimization (MOPSO), *Water resources management*, 27,
822 1931-1947, 2013.
- 823 Akhtar, T. and Shoemaker, C. A.: Multi objective optimization of computationally expensive multi-modal
824 functions with RBF surrogates and multi-rule selection, *Journal of Global Optimization*, 64, 17-32, 2016.
- 825 Alfonso, L., Jonoski, A., and Solomatine, D.: Multiobjective optimization of operational responses for
826 contaminant flushing in water distribution networks, *Journal of Water Resources Planning and Management*,
827 136, 48-58, 2010.
- 828 Amadori, M., Giovannini, L., Toffolon, M., Piccolroaz, S., Zardi, D., Bresciani, M., Giardino, C., Luciani, G.,
829 Kliphuis, M., and van Haren, H.: Multi-scale evaluation of a 3D lake model forced by an atmospheric model
830 against standard monitoring data, *Environmental Modelling & Software*, 139, 105017, 2021.
- 831 Ayala, A. I., Moras, S., and Pierson, D. C.: Simulations of future changes in thermal structure of Lake Erken:
832 proof of concept for ISIMIP2b lake sector local simulation strategy, *Hydrology and Earth System Sciences*,
833 24, 3311-3330, 2020.
- 834 Baracchini, T., Hummel, S., Verlaan, M., Cimatoribus, A., Wüest, A., and Bouffard, D.: An automated calibration
835 framework and open source tools for 3D lake hydrodynamic models, *Environmental Modelling & Software*,
836 134, 104787, 2020.
- 837 Bartlett, M., Parolari, A. J., McDonnell, J., and Porporato, A.: Beyond the SCS-CN method: A theoretical
838 framework for spatially lumped rainfall-runoff response, *Water Resources Research*, 52, 4608-4627, 2016.
- 839 Bartz-Beielstein, T. and Zaefferer, M.: Model-based methods for continuous and discrete global optimization,
840 *Applied Soft Computing*, 55, 154-167, 2017.
- 841 Beletsky, D., Schwab, D., and McCormick, M.: Modeling the 1998–2003 summer circulation and thermal
842 structure in Lake Michigan, *Journal of Geophysical Research: Oceans*, 111, 2006.
- 843 Chanudet, V., Fabre, V., and van der Kaaij, T.: Application of a three-dimensional hydrodynamic model to the
844 Nam Theun 2 Reservoir (Lao PDR), *Journal of Great Lakes Research*, 38, 260-269, 2012.
- 845 Coulon, C., Pryet, A., Lemieux, J.-M., Yrro, B. J. F., Bouchedda, A., Gloaguen, E., Comte, J.-C., Dupuis, J. C.,
846 and Banton, O.: A framework for parameter estimation using sharp-interface seawater intrusion models,
847 *Journal of Hydrology*, 600, 126509, 2021.
- 848 Davis, L.: *Handbook of genetic algorithms*, 1991.
- 849 Deltares: *Delft3D-FLOW user manual*, Deltares, Delft, the Netherlands 2014.
- 850 Elhakeem, A., Elshorbagy, W., and Bleninger, T.: Long-term hydrodynamic modeling of the Arabian Gulf,
851 *Marine Pollution Bulletin*, 94, 19-36, 2015.
- 852 Fabio, P., Aronica, G. T., and Apel, H.: Towards automatic calibration of 2-D flood propagation models,
853 *Hydrology and Earth System Sciences*, 14, 911-924, 2010.
- 854 Franco, A. C. L., Oliveira, D. Y. d., and Bonumá, N. B.: Comparison of single-site, multi-site and multi-variable
855 SWAT calibration strategies, *Hydrological Sciences Journal*, 65, 2376-2389, 2020.
- 856 Galelli, S., Castelletti, A., and Goedbloed, A.: High-Performance Integrated Control of water quality and quantity
857 in urban water reservoirs, *Water Resources Research*, 51, 9053-9072, 2015.
- 858 Gaudard, A., Schwefel, R., Vinnå, L. R., Schmid, M., Wüest, A., and Bouffard, D.: Optimizing the
859 parameterization of deep mixing and internal seiches in one-dimensional hydrodynamic models: a case study
860 with Simstrat v1. 3, *Geoscientific Model Development*, 10, 3411-3423, 2017.

861 Giuliani, M., Castelletti, A., Pianosi, F., Mason, E., and Reed, P. M.: Curses, tradeoffs, and scalable management:
862 Advancing evolutionary multiobjective direct policy search to improve water reservoir operations, *Journal*
863 *of Water Resources Planning and Management*, 142, 04015050, 2016.

864 Gupta, H. V., Kling, H., Yilmaz, K. K., and Martinez, G. F.: Decomposition of the mean squared error and NSE
865 performance criteria: Implications for improving hydrological modelling, *Journal of hydrology*, 377, 80-91,
866 2009.

867 Haftka, R. T., Villanueva, D., and Chaudhuri, A.: Parallel surrogate-assisted global optimization with expensive
868 functions—a survey., *Structural Multidisciplinary Optimization*, 54, 3-13, 2016.

869 Herman, J. D., Zeff, H. B., Reed, P. M., and Characklis, G. W.: Beyond optimality: Multistakeholder robustness
870 tradeoffs for regional water portfolio planning under deep uncertainty, *Water Resources Research*, 50, 7692-
871 7713, 2014.

872 Huang, A., Rao, Y. R., Lu, Y., and Zhao, J.: Hydrodynamic modeling of Lake Ontario: An intercomparison of
873 three models, *Journal of Geophysical Research: Oceans*, 115, 2010.

874 Hui, Y., Zhu, Z., and Atkinson, J. F.: Mass balance analysis and calculation of wind effects on heat fluxes and
875 water temperature in a large lake, *Journal of Great Lakes Research*, 44, 1293-1305, 2018.

876 Hydraulics, D.: *Delft3D-FLOW user manual*, Delft, the Netherlands, 2006.

877 Jin, K.-R., Hamrick, J. H., and Tisdale, T.: Application of three-dimensional hydrodynamic model for Lake
878 Okeechobee, *Journal of Hydraulic Engineering*, 126, 758-771, 2000.

879 Kaçıkoc, M. and Beyhan, M.: Hydrodynamic and water quality modeling of Lake Eğirdir, *Clean–Soil, Air, Water*,
880 42, 1573-1582, 2014.

881 Lu, D., Ricciuto, D., Stoyanov, M., and Gu, L.: Calibration of the E3SM land model using surrogate-based global
882 optimization, *Journal of Advances in Modeling Earth Systems*, 10, 1337-1356, 2018.

883 Luo, L., Hamilton, D., Lan, J., McBride, C., and Trolle, D.: Autocalibration of a one-dimensional hydrodynamic-
884 ecological model (DYRESM 4.0-CAEDYM 3.1) using a Monte Carlo approach: simulations of hypoxic
885 events in a polymictic lake, *Geoscientific Model Development*, 11, 903-913, 2018.

886 Marti, C. L., Mills, R., and Imberger, J.: Pathways of multiple inflows into a stratified reservoir: Thomson
887 Reservoir, Australia, *Advances in water resources*, 34, 551-561, 2011.

888 Odusanya, A. E., Mehdi, B., Schürz, C., Oke, A. O., Awokola, O. S., Awomeso, J. A., Adejuwon, J. O., and
889 Schulz, K.: Multi-site calibration and validation of SWAT with satellite-based evapotranspiration in a data-
890 sparse catchment in southwestern Nigeria, *Hydrology and Earth System Sciences*, 23, 1113-1144, 2019.

891 Parsapour-Moghaddam, P. and Rennie, C. D.: Calibration of a 3D hydrodynamic meandering river model using
892 fully spatially distributed 3D ADCP velocity data, *Journal of hydraulic engineering*, 144, 04018010, 2018.

893 Paturi, S., Boegman, L., Bouffard, D., and Rao, Y. R.: Three-dimensional simulation of Lake Ontario North-Shore
894 hydrodynamics and contaminant transport, *Journal of Hydraulic Engineering*, 141, 04014082, 2014.

895 Pelletier, G. J., Chapra, S. C., and Tao, H.: QUAL2Kw—A framework for modeling water quality in streams and
896 rivers using a genetic algorithm for calibration, *Environmental Modelling & Software*, 21, 419-425, 2006.

897 Pijcke, G.: *Water quality modelling for Gardens by the Bay*, Singapore, National University of Singapore, 2014.

898 Råman Vinnå, L., Wüest, A., and Bouffard, D.: Physical effects of thermal pollution in lakes, *Water Resources*
899 *Research*, 53, 3968–3398, 2017.

900 Razavi, S., Tolson, B. A., and Burn, D. H.: Review of surrogate modeling in water resources, *Water Resources*
901 *Research*, 48, W07401, 2012.

902 Reed, P. M., Hadka, D., Herman, J. D., Kasprzyk, J. R., and Kollat, J. B.: Evolutionary multiobjective optimization
903 in water resources: The past, present, and future, *Advances in water resources*, 51, 438-456, 2013.

904 Regis, R. G. and Shoemaker, C. A.: Combining radial basis function surrogates and dynamic coordinate search in
905 high-dimensional expensive black-box optimization, *Engineering Optimization*, 45, 529-555, 2013.

906 Solomatine, D. P., Dibike, Y. B., and Kukuric, N.: Automatic calibration of groundwater models using global
907 optimization techniques, *Hydrological Sciences Journal*, 44, 879-894, 1999.

908 Soullignac, F., Vinçon-Leite, B., Lemaire, B. J., Martins, J. R. S., Bonhomme, C., Dubois, P., Mezemate, Y.,
909 Tchiguirinskaia, I., Schertzer, D., and Tassin, B.: Performance Assessment of a 3D Hydrodynamic Model
910 Using High Temporal Resolution Measurements in a Shallow Urban Lake, *Environmental Modeling &*
911 *Assessment*, 22, 309-322, 2017.

912 Tasoulis, D. K., Pavlidis, N. G., Plagianakos, V. P., and Vrahatis, M. N.: Parallel differential evolution,
913 *Proceedings of the 2004 Congress on Evolutionary Computation (IEEE Cat. No. 04TH8753)*, 2023-2029,
914 Uittenbogaard, R. E., Van Kester, J. T. M., and Stelling, G. S.: Implementation of Three Turbulence Models in
915 TRISULA for Rectangular Horizontal Grids: Including 2DV-testcases, *Delft Hydraulics*1992.

916 Wagner, C. R. and Mueller, D. S.: Use of velocity data to calibrate and validate two-dimensional hydrodynamic
917 models, *Proceedings of the Second Federal Interagency Hydrologic Modeling Conference*,

918 Wahl, B. and Peeters, F.: Effect of climatic changes on stratification and deep-water renewal in Lake Constance
919 assessed by sensitivity studies with a 3D hydrodynamic model, *Limnology and Oceanography*, 59, 1035-
920 1052, 2014.

921 Wilson, H. L., Ayala, A. I., Jones, I. D., Rolston, A., Pierson, D., de Eyto, E., Grossart, H.-P., Perga, M.-E.,
922 Woolway, R. I., and Jennings, E.: Variability in epilimnion depth estimations in lakes, *Hydrology and Earth*
923 *System Sciences*, 24, 5559-5577, 2020.

924 Xia, W. and Shoemaker, C.: GOPS: efficient RBF surrogate global optimization algorithm with high dimensions
925 and many parallel processors including application to multimodal water quality PDE model calibration,
926 *Optimization and Engineering*, 22, 2741-2777, 10.1007/s11081-020-09556-1, 2021.

927 Xia, W. and Shoemaker, C. A.: Improving the speed of global parallel optimization on PDE models with processor
928 affinity scheduling, *Computer-Aided Civil and Infrastructure Engineering*, 37, 279-299, 2022a.

929 Xia, W. and Shoemaker, C. A.: A Repetitive Parameterization and Optimization Strategy for the Calibration of
930 Complex and Computationally Expensive Process-based Models with Application to a 3D Water Quality
931 Model of a Tropical Reservoir, *Water Resources Research*, 58, e2021WR031054, 2022b.

932 Xia, W., Shoemaker, C., Akhtar, T., and Nguyen, M.-T.: Efficient Parallel Surrogate Optimization Algorithm and
933 Framework with Application to Parameter Calibration of Computationally Expensive Three-dimensional
934 Hydrodynamic Lake PDE Models, *Environmental Modelling & Software*, 104910,
935 <https://doi.org/10.1016/j.envsoft.2020.104910>, 2021.

936 Xu, C., Zhang, J., Bi, X., Xu, Z., He, Y., and Gin, K. Y.-H.: Developing an integrated 3D-hydrodynamic and
937 emerging contaminant model for assessing water quality in a Yangtze Estuary Reservoir, *Chemosphere*, 188,
938 218-230, 2017.

939 Xue, P., Schwab, D. J., and Hu, S.: An investigation of the thermal response to meteorological forcing in a
940 hydrodynamic model of Lake Superior, *Journal of Geophysical Research: Oceans*, 120, 5233-5253, 2015.

941